Cell Reports
Physical Science

CellPress
OPEN ACCESS

Article

Closo-Hydroborate Sodium Salts as an Emerging Class of Room-Temperature Solid Electrolytes

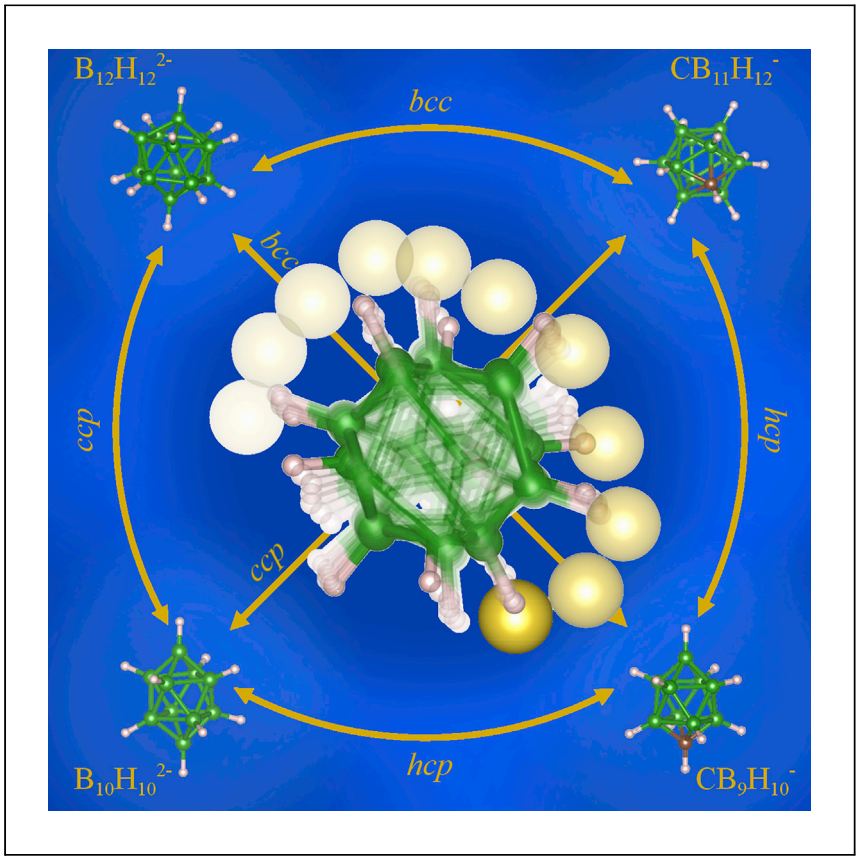

Various drawbacks limit the development of solid electrolytes for sodium-based batteries as cheap and efficient alternatives to conventional Li-ion batteries. Brighi et al. present a strategy to stabilize hydroborate-based compounds with high sodium mobility, large electrochemical and thermal stability, and excellent mechanical properties.

Matteo Brighi, Fabrizio Murgia, Radovan Černý

matteo.brighi@unige.ch (M.B.)
radovan.cerny@unige.ch (R.Č.)

HIGHLIGHTS

Suppression of structural phase transition in the 170 < T < 700 K range

Room-temperature Na conductivity about 1 mS cm^{-1} for all compounds

Oxidative stability up to 3 and 4 V versus Na^{+}/Na

Brighi et al., Cell Reports Physical Science *1*, 100217
October 21, 2020
https://doi.org/10.1016/j.xcrp.2020.100217

Please cite this article in press as: Brighi et al., *Closo*-Hydroborate Sodium Salts as an Emerging Class of Room-Temperature Solid Electrolytes, Cell Reports Physical Science (2020), https://doi.org/10.1016/j.xcrp.2020.100217

Cell Reports
Physical Science

Article

Closo-Hydroborate Sodium Salts as an Emerging Class of Room-Temperature Solid Electrolytes

Matteo Brighi,[1,2,*] Fabrizio Murgia,[1] and Radovan Černý[1,*]

SUMMARY

Na-based hydroborates, such as $NaCB_9H_{10}$, $Na_2B_{10}H_{10}$, $NaCB_{11}H_{12}$, and $Na_2B_{12}H_{12}$, are known for their high ionic conductivity above a phase transition, usually far from room temperature. Here, a systematic investigation to suppress this phase transition and thus to stabilize novel crystal structures is conducted by means of anion mixing. The obtained compounds crystallize either with hexagonal and cubic close packed (*hcp* and *ccp*) or body-centered cubic (*bcc*) arrangement of anions without polymorphic evolution in the temperature range 100 < T < 700 K. The high symmetry and the configurational ionic disorder, which characterize all crystals, give room-temperature Na^+ conductivity close or above 1 mS cm^{-1}. Finally, high oxidative electrochemical stability between 3 and 4 V versus Na^+/Na results from the aromatic nature of the boron cage, making Na-based hydroborates potentially suitable as efficient solid electrolytes for next-generation, high-voltage, Na-ion batteries.

INTRODUCTION

The biggest contemporary challenge in energy provision is the pursuit of energy storage systems capable of reversibly accumulating, storing, and providing on demand the amount of energy required by the grid. Li-ion batteries (LiBs) are undoubtedly the present, concrete contenders for powering portable devices but also automotive and domestic energy-storage systems. However, despite their flexibility, which allows them to be adapted from very low (e.g., smartwatches) to high power applications (e.g vehicles), LiBs still suffer from several major drawbacks. The increasing production will face a materials sustainability issue, due to the exploitation of cobalt.[1] Moreover, the impossibility of using metallic lithium as negative electrode hinders the increase of specific capacity and the limited electrochemical and thermodynamic stability of the liquid electrolyte (LE) represents a serious concern from a safety point of view.

All-solid batteries were proposed as a way to overcome these latter limitations. However, the initial enthusiasm was tempered by pioneering studies of Li and Na dendrite formation across solid ion conductors in the 1970s.[2]

It is still a matter of discussion to what extent solid electrolytes (SEs) can hinder electrolyte dendrite growth, because for different families of compounds do exist specific conditions for which dendrites form.[3] Nevertheless, SEs may still hold an advantage in terms of safety, as their higher specific heat compared to LEs could hinder hotspot formation as consequence of high current density output. For example, $Na_2B_{10}H_{10}$ has a specific heat of 305 J K^{-1} mol^{-1}, compared to only 140 and 173 J K^{-1} mol^{-1} at 320 K for ethylene carbonate (EC) and propylene carbonate (PC), respectively (E.M. Dematteis et al., 2018, 16th International Symposium on

[1]Laboratory of Crystallography, DQMP, University of Geneva, 24, quai Ernest-Ansermet, 1211 Geneva 4, Switzerland

[2]Lead Contact

*Correspondence: matteo.brighi@unige.ch (M.B.), radovan.cerny@unige.ch (R.Č.)

https://doi.org/10.1016/j.xcrp.2020.100217

Table 1. Theoretical Density of Several Ionic Conductors

Compound	Density (g cm^{-3})
EC[a]	1.32
PC[a]	1.21
$LiPF_6$[a]	2.84
$NaPF_6$[a]	2.53
$Li_{10}GeP_2S_{12}$	2.05
$Na_{11}Sn_2PS_{12}$	2.39
Na_3PS_4	2.21
$Li_7La_3Zr_2O_{12}$	4.91
Li_3PS_4	1.92
$LiBH_4$	0.66
$Na_2B_{12}H_{12}$	1.17

[a]Organic solvents or salts used in liquid electrolytes for LiB and post-LiB

Metal-Hydrogen Systems, conference).[4] They also have the potential to increase the specific capacity of the whole battery package if they can be developed with competitive densities resulting in SE lighter than conventional LE.

In order to offer a viable alternative to LEs, SEs should have a density lower than that of 1M of $NaPF_6$ dissolved in EC:PC, which has a density of 1.35 g cm^{-3}. This is particularly true in the case that SEs do not show better physical properties in terms of ionic conductivity (>1 mS cm^{-1}) or an electrochemical window wider than 3 V versus Li^+/Li (or Na^+/Na for sodium batteries).

The emergence of complex hydrides showing high ionic conductivity increased the number of possible SE candidate compounds. Several fundamental studies were done in order to explain the role of anion dynamic in the cation diffusion mechanism, for which those compounds feature ionic conductivity on the order of 1 mS cm^{-1}. Indeed, so far, several new hydroborate solid electrolytes have been successfully tested in electrochemical cells.[5–9] The low density of hydroborates, compared to those of phosphates and oxides (Table 1), makes it clear that the family of *closo*-deca- and dodeca-hydroborates (the deca- and dodeca-*carba*hydroborates have similar densities) represent an effective solution for increasing cell energy density.

Nevertheless, the fast ionic motion is triggered by a structural phase transition, characteristic of all alkali hydroborates, allowing their use only at temperatures higher than 363 K. Many efforts were done to stabilize the high temperature (HT) polymorph at room temperature (RT), via halide substitution, which mainly relies on the size effect, slightly varying the local ion-ion interactions.[6,10] A more useful strategy, however, is represented by alio- or isovalent anion mixing of the boron cluster *closo*-hydroborates, which maintains the same chemistry, avoiding the shrinkage of the electrochemical window, as observed for borohydrides, based on the $[BH_4]^-$ anion.[11] Several compounds obtained in this way, such as $Li_2(CB_9H_{10})(CB_{11}H_{12})$, $Na_4(B_{10}H_{10})(B_{12}H_{12})$, and $Na_3(CB_{11}H_{12})(B_{12}H_{12})$, showed not only high RT ionic conductivity but also do not have a structural phase transition over a very wide temperature range. These compounds are characterized by a high-symmetry, disordered, crystal structure.[8,12,13]

Hydroborates have been demonstrated to be rather electrochemically robust: Wiersema et al.[14] showed that the oxidative limit increases following the series

Please cite this article in press as: Brighi et al., *Closo*-Hydroborate Sodium Salts as an Emerging Class of Room-Temperature Solid Electrolytes, Cell Reports Physical Science (2020), https://doi.org/10.1016/j.xcrp.2020.100217

$[B_{10}H_{10}]^{2-}$ < $[B_{12}H_{12}]^{2-}$ < $[CB_9H_{10}]^-$ < $[CB_{11}H_{12}]^-$ (respectively at +0.4; +1.4; +1.85, and >+2.4 versus SCE). Due to the three-dimensional, aromatic-like electronic distribution in the anions, the hydroborates are also thermodynamically very stable and have been shown to be unchanged up to 873 K or even up to 1,073 K in the case of Cs-hydroborates.[15–17]

Starting from these prerequisites, a deeper investigation of the possible compounds that could be obtained by anion mixing seems a very promising route toward further generation of highly electrochemically stable solid electrolytes. In the following article, we present the series of Na-based compounds achieved by mixing the four above-mentioned *closo*-hydroborates. The crystal structures are discussed in relation to the ionic mobility and the electrochemical properties. A revisited solid-state-based investigation of the electrochemical stability is presented.

RESULTS

Crystal Structures

All single-anion compounds exist and crystallize as the high-temperature polymorph in one of the three common packing types, i.e., cubic close packing, hexagonal close packing, and body center cubic packing (*ccp*, *hcp*, and *bcc*), with an ionic conductivity higher than 1 mS cm^{-1} (see Table S1). At lower temperature, however, none of them keep the high-symmetry structure and an order-disorder phase transition occurs simultaneously with a drop of nearly three orders of magnitude in the anion reorientation rate (from 10^{11} to 10^8 s^{-1}).[18] As suggested by Kweon et al.,[19] the dynamics of polyanions and their modification (carbon substitution for boron or halide substitution for hydrogen) frustrate the structure, resulting in a flattening of the energy landscape for the mobile cation (Na^+ in this case).

From a structural point of view, locking off the anion rotation constrains the structure to deform to a lower symmetry subgroup, drastically limiting the long-range cation diffusion. The degree of lattice distortion (S) can be used as a measure of deformation.[20] In the four *closo*-hydroborate single anion compounds S = 6.49 × 10^{-2}, 3.12 × 10^{-2}, 1.85 × 10^{-2}, and 3.82 × 10^{-2} (see details in Note S1). When this is compared to a similar ionic conductor, such as AgI or Ag_2S with S = 0.256 and 0.170, respectively, the extent of the deformation can be seen to be rather small. This suggests that only a small increase of the entropy of mixing (or configurational entropy) due to the adoption of at least two different anions may stabilize the high-symmetry polymorph, as happens in the so-called high-entropy alloys.

Entropy, disorder, and frustration are the main ingredients in the design of superionic compounds:[21] this was indeed confirmed (for *closo*- and carba*closo*-hydroborates) by Tang et al.[22] and by Duchêne et al.[12] by means of mixing $NaCB_9H_{10}$ with $NaCB_{11}H_{12}$ and $Na_2B_{10}H_{10}$ with $Na_2B_{12}H_{12}$, respectively. Brighi et al. [13] explored in parallel another mixture and obtained a new phase with $NaCB_{11}H_{12}$ and $Na_2B_{12}H_{12}$.

To further confirm this approach, we systematically mixed *closo*-hydroborates and carba*closo*-hydroborates in a binary solution with a fixed stoichiometry 1:1 (Figure 1), which seems to be the only allowed ratio for isovalent mixing,[12,22] although aliovalent mixing allows higher stoichiometric flexibility.[13] In Figure 1, the packing characterizing the anion's sublattice for each mixture is shown. The anion's diversity is averaged out at high temperature by the increased dynamics,[23] making the net negative charge and thus the sodium concentration the key parameters defining a novel structure.

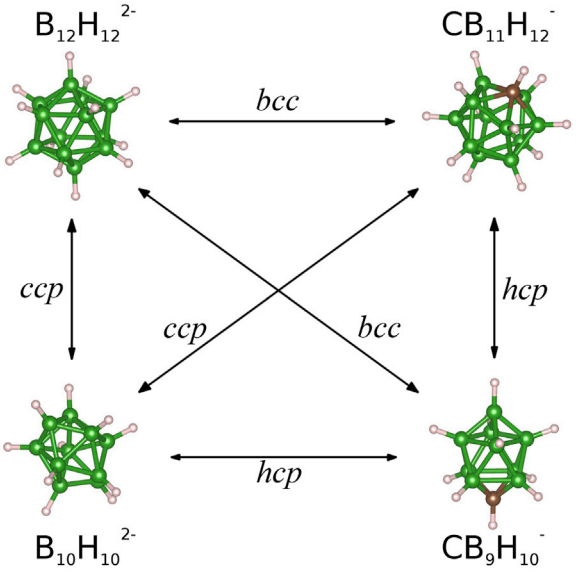

Figure 1. Structures of Polyanions

$[CB_9H_{10}]^-$, $[B_{10}H_{10}]^{2-}$, $[CB_{11}H_{12}]^-$, and $[B_{12}H_{12}]^{2-}$. Arrows indicate the mixture and resulting anion sublattice packing.

This new class of anion-mixed hydroborates is presented here below. For the sake of clarity, hereafter, when an anionic mixing is mentioned, it will be indicated as $[A_i–A_j]$ (A_i = CB_9, B_{10}, CB_{11}, B_{12}) and hydrogen labels will be omitted. As already demonstrated,[12,13,22] anion mixing stabilizes the high-symmetry polymorph at RT, regardless of the anionic charge (see Figure S1). The compounds will be presented according to their anion sublattice packing type. We will classify the given anion sublattice, possibly deformed, in that manner: (1) *ccp* or *hcp* if the anion-anion first coordination sphere has approximately the shape of a cuboctahedron or anti-cuboctahedron, respectively, and (2) *bcc* if the first coordination sphere has approximately cubic shape and the second coordination sphere forms approximately an octahedron. Moreover, the number and type of the interstitial sites as well as their connectivity must not change with respect to the ideal packing.

ccp Type

The isovalent mixture $[B_{10}$-$B_{12}]$ features a *ccp* sublattice, which exists in a distorted version as packing type of both RT $Na_2B_{10}H_{10}$ and $Na_2B_{12}H_{12}$. The choice of the space group (s.g.) *Fm*-3*m* as done by Duchêne et al.[13] also seems reasonable. Despite the complete disorder of anions (either dynamic or static), it was possible to refine Na atomic position and occupancy (the structure is presented in Figure 2A; RT *a* = 9.99752(3) Å; Rietveld plot in Figure S2). The Na positions converged to the same interstitial sites adopted for the HT-$Na_2B_{10}H_{10}$,[24] namely the Wyckoff sites 4*b*, 8*c*, and 24*d*. The refined occupancies, however, slightly differ from the pure $Na_2B_{10}H_{10}$, accumulating most of the Na on the tetrahedral 8*c* site, the most stable one when considering the first Pauling rule.

The second structure with a *ccp* anion sublattice is obtained in the aliovalent mixture $[B_{10}$-$CB_{11}]$. The resulting structure (visible in Figure 2B) crystallizes in an orthorhombic cell (s.g. *Pnnm*; RT lattice parameters *a* = 6.9407(8), *b* = 10.0192(2), and *c* = 6.9376(7) Å; Rietveld plot in Figure S3). Configurational and orientation disorder characterize the anions over the whole temperature range studied (170 < T < 540 K;

Cell Reports
Physical Science
Article

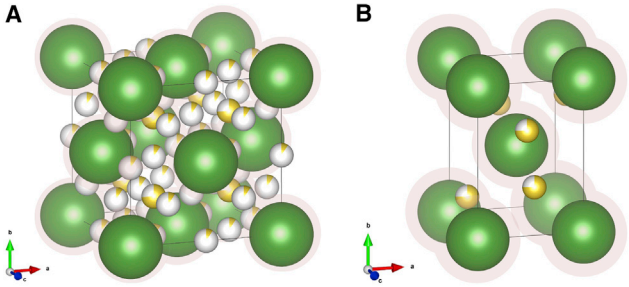

Figure 2. *ccp*-type Unit Cell

$[B_{10}\text{-}B_{12}]$ (A) and $[B_{10}\text{-}CB_{11}]$ (B). Na atoms are represented by yellow spheres (partial filling refers to the partial site occupancy), although to emphasize the orientation disorder, anions are replaced by a big green sphere (boron cage) and a pink shell (hydrogens).

see Figure S1), although Na^+ remains confined in the tetrahedral site (4*g* in s.g. *Pnnm*). For both structures, the anti-CaF_2 structure type was chosen as the aristotype.

In terms of the chemical stability, *in situ* X-ray diffraction (XRD) and differential scanning calorimetry (DSC) demonstrated no thermal decomposition/reaction in a range $100 < T < 730$ K (Figures S1 and S4).

The results from $[B_{10}\text{-}CB_{11}]$ are intimately related to those of $[B_{10}\text{-}B_{12}]$. Indeed, orienting $[B_{10}\text{-}CB_{11}]$ along <101> in the <100 > direction of $[B_{10}\text{-}B_{12}]$, the anion lattice overlaps apart from a small volume contraction of $\Delta V/V \sim 3.6\%$, obviously related to the lower Na content in the aliovalent structure. The displacements of the tetrahedral Na positions, compared to the ideal *ccp* phase, have an amplitude ranging from 0.68 to 0.76 Å. In Figure S5, these two unit cells are superimposed, with overlapping anion positions. Only the Na atoms (color coded for each phase) are drawn, showing the mutual displacement.

hcp Type

The second close packing (*hcp*) is obtained in the mixture $[CB_9\text{-}B_{10}]$ and $[CB_9\text{-}CB_{11}]$ (shown in Figure 3). The two structures proposed share the same s.g. *P*31*c*, a choice due to lower refinement quality with higher symmetry (Rietveld plots in Figures S6 and S7 for $[CB_9\text{-}B_{10}]$ and $[CB_9\text{-}CB_{11}]$, respectively). The same symmetry was adopted by Tang et al.[25] in describing the disordered phase of $NaCB_9H_{10}$. The RT lattice parameters are $a = 6.9887(9)$ and $c = 11.2783(7)$ Å for $[CB_9\text{-}B_{10}]$ and $a = 6.8524(0)$ and $c = 10.9394(4)$ Å for $[CB_9\text{-}CB_{11}]$.

The geometrical center of disordered hydroborate lies on the 2*b* Wyckoff site in both structures. Na atoms in $[CB_9\text{-}B_{10}]$ partially fill 2*a* and 2*b* Wyckoff sites, corresponding to octahedral and tetrahedral sites, respectively. $[CB_9\text{-}CB_{11}]$, being formed of only monovalent anions, has a lower Na content, and this constrains sodium to occupy only the tetrahedral 6*c* site. This latter is a general position and mimics the Na disorder around the 3-fold axis. As in the case of *ccp*-type structures, the Na positions match each other very well in both compounds (Figure S5). The structural aristotype is ZnS-wurtzite.

Unexpectedly, the more Na-rich phase ($[CB_9\text{-}B_{10}]$) has smaller volume/formula unit than $[CB_9\text{-}CB_{11}]$, showing a volume contraction of $\Delta V/V \sim 7.2\%$ (Table S2). Contrary to other systems where stuffing (emptying) the unit cell with additional (fewer) cations (i.e., by doping) leads to a volume expansion (contraction), in this case, the

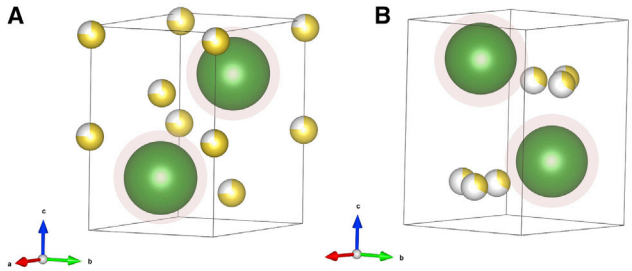

Figure 3. *hcp*-type Unit Cell

$[CB_9\text{-}B_{10}]$ (A) and $[CB_9\text{-}CB_{11}]$ (B). Na atoms are represented by yellow spheres (partial filling refers to the partial site occupancy), although to emphasize the orientation disorder, anions are replaced by a big green sphere (boron cage) and a pink shell (hydrogens).

Na content is not the only parameter controlling the cell volume. Here, the anion volume plays an important role. This feature was also observed for the mixture $[CB_{11}\text{-}B_{12}]$,[13] and it will be described in the next section.

Hence, in terms of size, the deca-hydroborate, with a symmetry D_{4d}, is smaller than dodeca-hydroborate (icosahedral symmetry I_h) in the plane perpendicular to its 4-fold axis. Despite the dynamical disorder that tends to average all geometry anisotropies, the disordered deca-hydroborate results in the smaller cell volume of the Na-rich phase. Both phases show no phase transition in the whole studied temperature range (see Figure S1), whereas a significant mass loss coupled with irreversible peaks in DSC was observed for each structure above 700 K (see Figure S4).

bcc Type

Finally, the *bcc* packing is obtained for the mixture $[CB_9\text{-}B_{12}]$ and $[CB_{11}\text{-}B_{12}]$. Although the latter is properly cubic, with a RT unit cell parameter a = 7.9293(7) Å (s.g. *I*23), the more polar CB_9 slightly deforms the lattice to a tetragonal symmetry: a = 7.7982(0); c = 7.8077(2) Å (s.g. $P\text{-}42_1c$). The two structures (shown in Figure 4; Rietveld plots in Figures S8 and S9 for $[CB_9\text{-}B_{12}]$ and $[CB_{11}\text{-}B_{12}]$, respectively) clearly show anion disorder already at RT. In this case, Na distribution is also similar for the two structures (Figure S5). In $[CB_9\text{-}B_{12}]$, sodium occupies the 6*c* Wyckoff site, forming squares around the *c* axis, although in $[CB_{11}\text{-}B_{12}]$, it is on 12*e* site, where the distribution is no longer slab-like but three-dimensional, approaching the Ag-conduction topology in the α-AgI.[26] For the structural aristotype, the HT polymorph $\alpha\text{-}Ag_{1.5}(S_{0.5}I_{0.5})$ is preferred because of the anion mixing.[27] The *bcc* packing in Na-hydroborates has also been obtained very recently by mixing the *nido* and *closo* polyanions $[B_{11}H_{14}]^-$ and $[B_{12}H_{12}]^{2-}$.[28]

Interestingly, regarding the volume/formula unit (summary in Table S2), one can observe that, as mentioned above, no correlation exists with the amount of sodium contained in the unit cell (from 1 to 2 Na per anion). As discussed in a previous work on $[CB_{11}\text{-}B_{12}]$, tuning the anions ratio, i.e., the Na content, does not affect the cell volume.[13] Also, anion disorder can be deduced when comparing the volume/formula unit for each mixture with the averaged value obtained using ordered single-anion *closo*- and carba*closo*-hydroborates (Table S2). It can be noticed that very little difference exists for dodecahedrons polyanions, although all the other mixtures have larger deviations from the averaged values. These discrepancies are likely related to decahedrons and can be explained in terms of the anions dynamical disorder (furthermore experimentally observed by XRD). Being deca-hydroborates ellipsoids, when randomly oriented around their geometrical center,

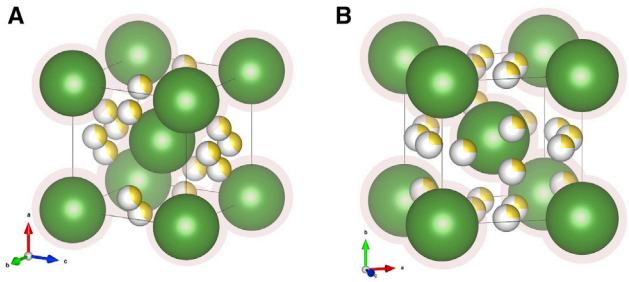

Figure 4. *bcc*-type Unit Cell

$[CB_9\text{-}B_{12}]$ (A) and $[CB_{11}\text{-}B_{12}]$ (B). Na atoms are represented by yellow spheres (partial filling refers to the partial site occupancy), although to emphasize the orientation disorder, anions are replaced by a big green sphere (boron cage) and a pink shell (hydrogens).

they approach a spherical shape (with the major axis as radius), resulting in a bigger volume.

In order to exclude a possible anion ordering in $[CB_{11}\text{-}B_{12}]$, which is in practice not visible by XRD due to the poor contrast between the carbon and boron, RT neutron diffraction was conducted on a partly deuterated $[CB_{11}\text{-}B_{12}]$ sample, where only the B_{12} anion was deuterated. The absence of any superstructure peaks (Figure S10) excludes any long-range ordering of anions down to RT. Combining the results obtained by XRD and DSC, there are no phase transitions in a broad temperature range (170 K < T < 700 K; see Figures S1 and S4), supporting the assumption that structural disorder occurs, in this temperature range, in all herein presented mixed compounds.

Na Dynamics

The Na^+ conductivity was studied by means of electrochemical impedance spectroscopy (EIS) in a frequency range $10^{-2} < f < 10^7$ Hz, spanning a temperature range from 170 K to 450 K. The DC ionic conductivity as function of 1/T is shown in Figure 5A. These values are determined from the real part of the electrical conductivity (graphs reported in Figure S11). The almost frequency-independent part of the spectra, defining a plateau, indicates a single ion diffusive process, although at higher frequency, the system enters the so-called nearly constant loss (NCL) dispersive regime.[29] Complementary, all spectra were fitted on the Nyquist plot by means of the equivalent circuit that better explains the data (Figures S12 and S13; Table S3).

With the exception of $[CB_{11}\text{-}B_{12}]$, all mixed compounds show the appearance of a second plateau at temperature below 190 K. This is likely due to a cumulative effect of high impedance of the sample's response and instrumental high-frequency noise. A secondary contribution to the ion relaxation, usually assigned to grain boundaries, must be excluded in the first instance due to the absence of it in the mixture $[B_{10}\text{-}B_{12}]$ measured by Duchêne et al.[30] and second because usually it appears at lower frequency than the bulk conductivity.[31] As shown in Table S3, at RT, none of these contributions are visible in the measured frequency range, although at 190 K (where both are detectable), their capacitance amount to tenth of nF, usually too small for grain boundary contribution.[31]

Figure 5A reveals two important features. The first, highlighted by the green box defining the region $\sigma > 1\text{mS cm}^{-1}$ and T > RT, is that all mixtures are already superionic at RT with the exception of $[B_{10}\text{-}B_{12}]$ and $[B_{10}\text{-}CB_{11}]$ (which, however, reach the superionic regime at 313 and 323 K, respectively). This demonstrates that, besides

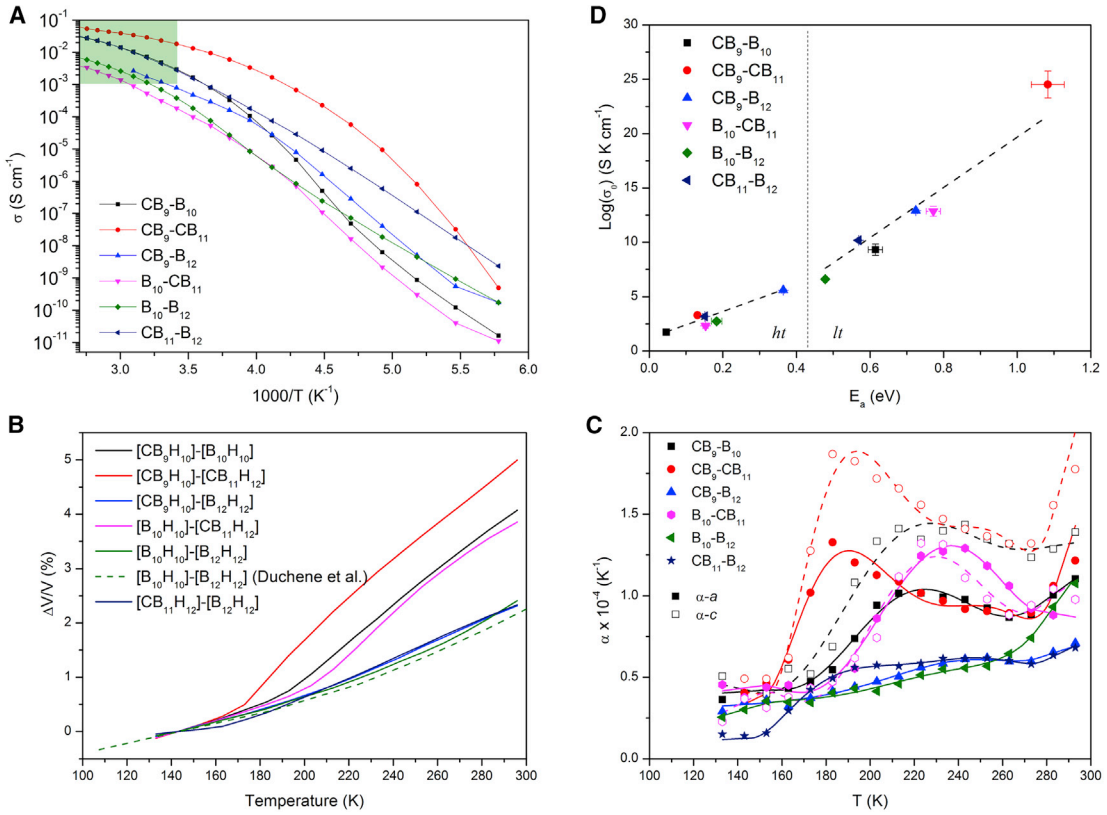

Figure 5. Temperature Dependence of the Ionic Conductivity and Lattice Parameters

(A) Arrhenius plot of Na conductivity of all mixtures.

(B and C) Respectively, the unit cell percent volume expansion and the linear thermal expansion coefficient. In the latter, for non-cubic structures, both *a* and *c* parameters are shown with filled and empty symbols, respectively.

(D) Meyer-Neldel plot of the conductivity prefactor σ0 as a function of the activation energy E_a. The error bars represent the fit's standard deviation.

the stabilization of the high symmetry structure, remarkably, anion mixing leads also to a liquid-like Na mobility. The second feature that should be noted is the non-Arrhenius dependency of the ionic conductivity. This physical aspect has been exhaustively investigated by Duchêne, where the concept of the coupling model (CM)[32] was successfully applied on the system [B_{10}-B_{12}].[30] The many-body nature of ion-ion interaction at intermediate temperature (232 < T < 323 K for [B_{10}-B_{12}]) leads to an increased activation energy (E_a*) at temperatures below a glass-like transition observed by DSC. According to the CM, E_a* is related to the activation energy of single-body relaxation (E_a in Debye model, where no interactions are present among dipoles, typical of high temperature) by the relation $E_a^* = E_a/(1 - n)$, with *n* the coupling parameter in the CM, a fraction of unity that increases with the interaction strength. The non-Arrhenius behavior of all curves of Figure 5A suggests the same feature as observed for [B_{10}-B_{12}], however showing several differences depending on the mixture considered. From the structural study presented above, anomalies of the volume expansion were observed at temperatures lower than 220 K (Figure 5B). Such discontinuity becomes evident for all mixtures, defining different temperature regions, when regarding the linear thermal expansion coefficient α (Figure 5C). A glass transition shows a jump of the specific heat c_p across the transition temperature T_g, and the same is true for α, which is c_p dependent.[33]

Please cite this article in press as: Brighi et al., *Closo*-Hydroborate Sodium Salts as an Emerging Class of Room-Temperature Solid Electrolytes, Cell Reports Physical Science (2020), https://doi.org/10.1016/j.xcrp.2020.100217

Table 2. Values of Activation Energy E_a Found from Fitting

	Low T E_a (meV)	High T E_a (meV)	*n*
$[CB_9\text{-}B_{10}]$	0.615	0.046	0.92
$[CB_9\text{-}CB_{11}]$	1.083	0.131	0.88
$[CB_9\text{-}B_{12}]$	0.724	0.364	0.50
$[B_{10}\text{-}CB_{11}]$	0.772	0.153	0.80
$[B_{10}\text{-}B_{12}]$	0.514	0.299	0.42
$[CB_{11}\text{-}B_{12}]$	0.569	0.151	0.73

Fitting were performed in both low and high temperature range, using the formula $\ln(\sigma T) = A - E_a/k_bT$, where A is a constant and k_b is the Boltzmann constant. The third column lists the value of the coupling parameter *n* obtained as described in the text.

A glass-like transition is confirmed for all mixtures with the transition onset lying between 150 and 200 K, depending on the mixture. An investigation of the Na dynamics on a microscopic level is beyond the scope of this work and is the subject of on-going investigations. However, the presented family of compounds encompass all the necessary aspects to flatten the Na energy landscape, as recently discussed by Kweon et al.[19] in terms of structural, chemical, and dynamical frustration. These six mixtures, in which a non-negligible ion-ion interaction is present at low temperature, exhibit a steady Na diffusion with low E_a at RT. E_a has been determined using a crude approximation from a linear fit of $ln(\sigma T)$ versus 1/T over the temperature range where the conductivity shows an Arrhenius behavior. The values are reported in Table 2. The importance of this finding is that, not only do all mixtures have a conductivity higher than 1 mS cm^{-1} at/or close to RT but also that the activation energy at this temperature is comparable to those of HT polymorphs of single anion phases, either Li or Na-based *closo*-hydroborates.[34]

The coupling parameter *n* for $[B_{10}\text{-}B_{12}]$ mixture is found to be 0.42, in excellent agreement with the value observed by Duchêne et al.[30] (0.40). We can extend the same discussion to the other mixtures, identifying three distinct regions of conductivity. The first is confined to temperatures below the glass-like transition temperature. The second corresponds to the intermediate regime, above the glass-like transition up to temperatures close to/or above RT, where the CM model explains the correlated cation-anion motion. And finally, a third region is where the thermal energy is high enough to decouple the cation motion from the anion dynamics and make any dynamic fluctuation in the energy landscape given by the anion libration negligible.

The resulting E_a and *n* are shown in Table 2. The results from these six different anion combinations could shed light on the dynamic nature of the cation-anion correlation, because the strength of such interaction is related to the choice of anion pairs (different *n* values). Anion-anion correlation could also play a role; indeed, we observed that the mixtures containing the lowest *n* all share the spherical-like and non-polarized $[B_{12}H_{12}]^{2-}$.

A final remark arises from the observation of the so-called Mayer-Neldel (MN), or compensation, rule. In Figure 5D, the $\log(\sigma_0)$ versus E_a is plotted in both the high- and low-temperature regimes (with respect to the glass transition). This finding is in agreement with the CM, which states that different ionic conductors with approximately the same E_a and ion jump-attempt frequency ($1/\tau_\infty$) can obey the MN rule by differing in the coupling parameter *n*.[35] This is in agreement with the results shown in Table 2. Another interpretation of the MN rule by Yelon et al.[36] relates the slope of

the MN plot to the entropy of migration and hence to the lattice Debye frequency (ω_D). More recently, Kraft and Culver[37,38] applied this concept to a series of argyrodite and thiophosphate-based ionic conductors, showing that a stiffer lattice exhibits a flatter MN slope. Here, we can identify two different slope regions (linear fits in Figure 5D), which correspond, respectively, to temperatures higher and lower than the glass transition. Hazen et al.[39] demonstrated how cation disorder changes the elastic properties of magnesium titanate ($MgTi_2O_5$), resulting in a lower bulk modulus in the disordered structure. This is due to different compressibility of the MgO_6 and TiO_6 octahedra in the ordered phase, although an averaged value is a consequence of disorder. In the mixed-anion presented here, one can imagine the same situation given by an occupied and a vacant tetrahedral Na site. These sites are frozen below the glass transition, although an averaged, isotropic occupation will occur above the transition temperature.

Thus, from the MN plot, we expect a softening of the crystal at low temperatures. Ongoing efforts to obtain single crystals of such structures will hopefully enable a complete mechanical characterization and also confirm this peculiar feature.

Electrochemical Stability

The operating window of a solid electrolyte (i.e., the voltage range where the material does not undergo electrochemical reactions) is a key parameter to optimize in progress toward achieving marketable high-energy density batteries. Integration of high-voltage operating positive electrodes is mainly hindered by the oxidative electrochemical stability of the electrolyte. Therefore, the oxidative operational limit of each binary mixture was studied by means of slow-scan-rate cyclic voltammetry (SSRCV). Solid-state electrochemical reactions require the use of slow-voltage scan rates. This is due to the slow kinetics of the decomposition products, as well the lack of diffusivity toward the working electrode, compared to conventional CVs, in which electroactive species can more efficiently diffuse throughout the cell. As a consequence, it is necessary to tune the setup in order to perform optimized measurements, slowing the voltage scan rate, adding conductive non-interfering materials in the analyzed sample or using highly sensitive current analysis devices. Indeed, performing CV measurements in all-solid-state systems without any appropriate tuning can lead to dramatically weakened signals that are indistinguishable from the baseline noise. Several outstandingly wide electrochemical windows that were claimed for different Li- and Na-based solid-state electrolytes have since been revisited with more appropriate setups, leading to the determination of narrower, more realistic operating voltage windows.[11,24,40,41] Figure 6 reports the SSRCV measurement for the six analyzed compounds. The detected peaks are listed in Table 3.

From the comparison of the three [CB_9]-containing mixtures (Figures 6A–6C), a common peak around 3.75/3.8 V is visible in 2 out of 3 curves, however is barely noticeable in [CB_9-B_{12}] sample. This peak can be tentatively assigned to the oxidation of the common anion, $[CB_9H_{10}]^-$. This value is surprisingly low compared to the previous studies dealing with the oxidative stability of $[CB_9H_{10}]^-$ ions dissolved in acetonitrile, which was found to be at 4.8 V versus Na^+/Na.[14] However, the value here reported is consistent with a more recent study on similar solid-state cells, featuring $Li_2(CB_9H_{10})(CB_{11}H_{12})$ as electrolyte.[42] Figures 6A, 6D, and 6E show the SSRCVs of the [B_{10}]-containing compounds. A major peak centered around 3.42–3.52 V is observed for all the three mixtures, indicating the decomposition of the $[B_{10}H_{10}]^{2-}$ anion. Unlike [CB_9]-containing compounds, this result matches well with the observations on the oxidation of the anion in non-aqueous solutions, in which the

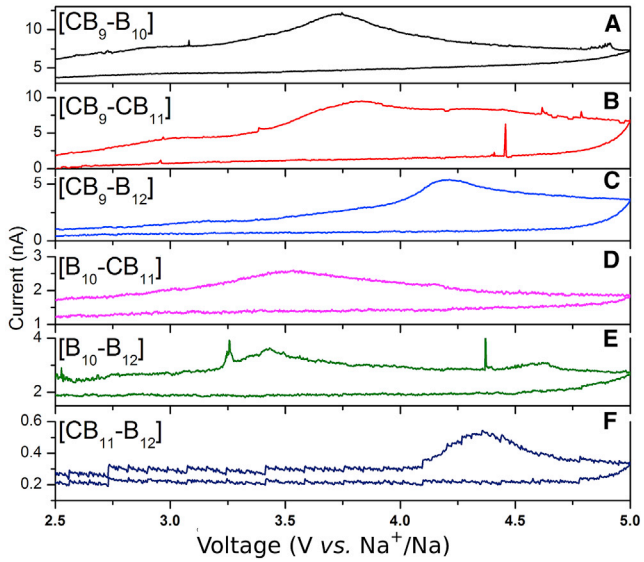

Figure 6. Oxidative Stability of the Mixed-Anion Structures
All curves were obtained with a scan rate of 20 μV s^{-1} and at temperature of 333 K.

potential, depending on the concentration, ranges from 3.38 to 3.44 V versus Na^+/Na.[43] $[CB_{11}]$-containing mixtures are depicted in Figures 6B, 6D, and 6F. Here, similarly to the case of $[CB_9H_{10}]^-$ anions, the oxidation of $[CB_{11}H_{12}]^-$ that was not noticed up to 5.35 V versus Na^+/Na in acetonitrile solutions can be tentatively assigned to approximately 4.2 V versus Na^+/Na. Such assignments are not straightforward due to the differences in the peak intensities between the samples. Lastly, Figures 6C, 6E, and 6F sum up the $[B_{12}H_{12}]^{2-}$ compounds, where, with the exception of $[B_{10}$-$B_{12}]$, main peaks around 4.1–4.2 V indicate the decomposition of $[B_{12}H_{12}]^{2-}$ ion. Moreover, in the sample $[CB_{11}$-$B_{12}]$, the 4.2 V peak appears broadened, compared to that in $[CB_9$-$B_{12}]$ sample. This could be attributed to the superposition of the two decomposition signals: the first of $[B_{12}H_{12}]^{2-}$ anion, followed by those of $[CB_{11}H_{12}]^-$, thereby reinforcing the analysis made for the $[CB_{11}H_{12}]^-$ oxidation. This is further supported by a similar value measured in a tetraglyme $Mg(CB_{11}H_{12})_2$ solution.[44] Summarizing the results of the SSRCV (see Table 3), it is possible to state that the oxidation of each mixture, which indicates their operational voltage window in a battery, is mainly related to the oxidation stability of the single component in the mixture. In other words, the anion that undergoes oxidation first sets the practical stability limit of the whole binary compound. However, a minor but non-negligible contribution in the energy landscape change, due to the mixing of the anion, could be responsible for the small shift on the oxidation values measured for the same anion gathered in different mixtures.[13] Lastly, it is worth noting that the decomposition voltage of the non-carbonated species is in better agreement with the literature, although dramatic shift toward lower potentials is observed for carba-*closo* anions. Nonetheless, sorting the anions as a function of their oxidation voltage, from lowest to highest, i.e., $[B_{10}H_{10}]^{2-}$, $[CB_9H_{10}]^-$, $[B_{12}H_{12}]^{2-}$, and $[CB_{11}H_{12}]^-$, it is arguable that the stability increases as the cage size increases. This trend is in good agreement with previous reports on the excellent "aromatic-like" stability of $[B_nH_n]^{2-}$ *closo*-anions, which is due to the increased delocalization of the B-B σ–bonds in the polyhedral clusters.[45,46] In addition, from the determination of the anion stability as a function of the resonance energy (β), $[B_{12}H_{12}]^{2-}$ appears the most stable of the series. Interestingly, although β is stable or slightly increasing between $[B_6H_6]^{2-}$ and $[B_{10}H_{10}]^{2-}$, it almost doubles between $[B_{10}H_{10}]^{2-}$ and $[B_{12}H_{12}]^{2-}$. This demonstrates

Table 3. Onset of the Electrochemical Events Visible in Figure 6

	$[B_{10}]^{2-}$	$[CB_9]^-$	$[B_{12}]^{2-}$	$[CB_{11}]^-$
$[CB_9\text{-}B_{10}]$	3.44	3.72		
$[CB_9\text{-}CB_{11}]$		3.82		4.32
$[CB_9\text{-}B_{12}]$		3.84	4.20	
$[B_{10}\text{-}CB_{11}]$	3.51			4.16
$[B_{10}\text{-}B_{12}]$	3.43		4.61	
$[CB_{11}\text{-}B_{12}]$			4.36	

The values are grouped according to the assumed anion decomposition.

the superior stability of 12-vertex polyhedra compared to all other cages[47] and highlights that the anion stability is mainly due to the isotropic delocalization of σ electrons. Moreover, C-containing anions seem to be more robust than their corresponding *closo* compounds. This could be due to the different acidity of the C-H hydrogen, which, unlike $[B_nH_n]^{2-}$ compounds, is comparable with those of acetylene.[48] A higher acidity corresponds to a higher stability of the conjugated base; therefore, the corresponding anion is less prone to oxidation, leading to a higher decomposition voltage for the C-substituted anions with respect to their unsubstituted counterparts.

DISCUSSION

A systematic investigation of all possible binary mixtures of the precursors $NaCB_9H_{10}$, $Na_2B_{10}H_{10}$, $NaCB_{11}H_{12}$, and $Na_2B_{12}H_{12}$ was carried out, leading to six novel phases in the context of solid Na-ion conductors.

All of these new compounds show a high-symmetry anion sublattice, which is thermodynamically stable over a wide temperature range without any phase transition. This dramatic difference compared to the behavior of the listed precursors opens new possibilities for employing hydroborates in RT solid state batteries applications. All three basic anions packing, *ccp*, *hcp*, or *bcc*, show similar Na-ion conductivity. A peculiar aspect that needs to be further investigated is the non-Arrhenius behavior of the Na conductivity. This hints at the complexity of the anion-anion and anion-cation interactions as function of their dynamics. This is more difficult to study in the precursors because ionic motion is triggered by a structural phase transition. The presence of a glass-like transition below 220 K means there is a Na liquid-like mobility and, indeed, all mixtures are already above, or close to, the 1 mS cm^{-1} at RT.

The electrochemical robustness of the presented compounds was demonstrated, and an oxidative window between 3 and 4 V versus Na^+/Na was found, depending on the choice of the anion pair. The electrochemical oxidation of each mixed phase is controlled by the stability of the single anion with the lowest stability toward oxidation. Therefore, by listing all anions according to their oxidative limit, i.e., $[B_{10}H_{10}]^{2-} < [CB_9H_{10}]^- < [B_{12}H_{12}]^{2-} < [CB_{11}H_{12}]^-$ is it possible to conclude that $[CB_9\text{-}B_{10}]$ represents the less stable mixture and $[CB_{11}\text{-}B_{12}]$ the most stable one.

These observations highlight that the main parameter in determining the anion stability is the size of the cage, with a significant difference between 10- and 12-vertex polyhedra. On the other hand, the C substitution and the consequent difference in the proton acidity of the C-H vertex, although improving its nucleophilic character (i.e., its stability toward oxidation), seems to only slightly raise the decomposition voltage.

Cell Reports
Physical Science
Article

CellPress
OPEN ACCESS

As consequence of these findings, an increase of interest in the scientific community is expected in order to investigate the fundamental theoretical aspects of such structures in more detail. Due to their large oxidative window and low gravimetric density, this family of compounds represents a substantial breakthrough in the search for feasible solid electrolytes in all-solid rechargeable batteries.

EXPERIMENTAL PROCEDURES

Resource Availability

Lead Contact

Further information and requests for resources should be directed to and will be fulfilled by the Lead Contact, Matteo Brighi (matteo.brighi@unige.ch).

Materials Availability

This study did not generate new unique reagents.

Data and Code Availability

All of the key data supporting the findings of this study are presented within the article and the Supplemental Information. Details of the crystal structure investigations may be obtained from the Fachinformationszentrum Karlsruhe, 76344 Eggenstein-Leopoldshafen (Germany), on quoting the depository numbers CSD-2005702, CSD-2005703, CSD-2005704, CSD-2005705, CSD-2005706, CSD-2005707. All other data are available from the Lead Contact upon reasonable request.

Synthesis

All Na-based *closo*- and carba*closo*-hydroborates, namely $NaCB_9H_{10}$, $Na_2B_{10}H_{10}$, $NaCB_{11}H_{12}$, and $Na_2B_{12}H_{12}$, were purchased at Katchem and dried overnight (at least 12 h) at 473 K under dynamic vacuum ($\sim 10^{-3}$ mbar). All the mixtures were synthesized mechanochemically in a planetary mill Fritsch P7 at 500 rpm for 2 h (2 min mill, 2 min break, 30 cycles). The only exception was for the mixture [B_{10}-B_{12}], which does not react completely, and coexistence of both *ccp* and *bcc* phases were observed (see Figures S1E and S14). Although the *ccp* likely corresponds to the effective mixture, the *bcc* structure is probably $Na_2B_{12}H_{12}$ and could be the result of pressure-induced stabilization by ball milling, as the high pressure polymorphs forms at relatively low pressure.[49] However, increasing the milling energy, by the adoption of three-dimensional shaker SPEX 8000, the homogeneous mixture was obtained. We point out that, among the other mixtures, also [CB_9-B_{12}] forms in such way.

After milling, all mixtures were heated for at least 12 h at 473 K under dynamic vacuum ($\sim 10^{-3}$ mbar) to improve crystallinity.

Structural Characterization

The analysis of distortion modes (Note S1) for the polymorphic evolution of $NaCB_9H_{10}$, $Na_2B_{10}H_{10}$, $NaCB_{11}H_{12}$, and $Na_2B_{12}H_{12}$ was conducted by means of the software AMPLIMODE,[50,51] available in the Bilbao Crystallographic Server. When group-subgroup relation did not exist, a lower symmetry equivalent structure was created based only on the anion sublattice, allowing a correct group-subgroup path. Alternatively, in the case of *bcc* branch of $Na_2B_{12}H_{12}$, the utility STRAIN was used to determine the degree of lattice distortion S.

The crystal structures of the presented compounds were studied by means of synchrotron powder XRD, and the data were collected at Swiss Norwegian Beamline (ESRF) with a wavelength of 0.77936 Å in a temperature range $170 < T < 770$ K.

The $[CB_9\text{-}B_{10}]$ compound was further studied and measured at Materials Sciences-beamline of Swiss Light Source at Paul Scherrer Institute with a wavelength of 0.70952 Å. One pattern measured with laboratory source ($\lambda = Cu_{K\alpha 1}$) was collected at RT to refine the structure of $[B_{10}\text{-}B_{12}]$ on a Panalytical Empyrean (Debye-Scherrer geometry) equipped with a PIXcell3D detector.

The powder patterns were indexed with Fox,[52] and the structures were solved *ab initio* by Fox in the s.g. mentioned in the section "Crystal Structures." The obtained structural models were then refined with the Rietveld method using the program TOPAS,[53] constraining the polyanions to only rotate around their geometrical center. Because the latter always comes to lie on a special position, the polyanions are disordered in all cases because the site symmetry (C_3, C_3, S_4, C_{2h}, O_h, and O_h for $[CB_9\text{-}B_{10}]$, $[CB_9\text{-}CB_{11}]$, $[CB_9\text{-}B_{12}]$, $[B_{10}\text{-}CB_{11}]$, $[B_{10}\text{-}B_{12}]$, and $[CB_{11}\text{-}B_{12}]$, respectively) is incompatible with the polyhedral symmetry (C_{4v}, D_{4d}, C_{5v}, and I_h for $[CB_9H_{10}]^-$, $[B_{10}H_{10}]^{2-}$, $[CB_{11}H_{12}]^-$, and $[B_{12}H_{12}]^{2-}$). For this reason and because of the poor boron/carbon scattering power contrast, only one polyanion (dodeca-hydroborate) was adopted in the structural model. Only for $[CB_9\text{-}B_{10}]$ and $[CB_{11}\text{-}B_{12}]$ is the reality approached by using deca-hydroborate and dodeca-hydroborate polyanions, respectively. All structural drawings were done with the program VESTA.[54]

In order to exclude any superstructure formation, due to ordering of different polyanions, practically invisible from XRD, neutron diffraction was performed with the mixture $[CB_{11}\text{-}B_{12}]$.

$Na_2B_{12}H_{12}$ was deuterated as a precursor for the mixture. Isotopic exchange was obtained under 5-MPa deuterium back pressure at 700 K for 5 h. The procedure was repeated several times in order to maximize the exchange efficiency. A successful substitution of 44 mol % was determined by Raman spectroscopy (Figure S15) by calculating the ratio of the integrated relative intensity of the B-H and B-D stretching mode.

The deuterated *closo*-hydroborate was then mixed in 1:1 molar ratio with $NaCB_{11}H_{12}$ as described above. Time-of-flight (TOF) experiments were performed on the NOVA spectrometer at the Material and Life Science Experimental Facility (MLF), at the Japan Proton Accelerator Research Complex (J-PARC). The sample was filled in a cylindrical null-scattering $V_{96}Ni_4$ alloy sample container with outside diameter of 6 mm and thickness of 0.10 mm. Data were collected up to Q_{max} = 107.79 $Å^{-1}$.

DSC measurements were performed in the department of Physical Chemistry of the University of Geneva, in a Netzsch DSC 404 F3 Pegasus calorimeter, in aluminum crucibles and under protective nitrogen flow (20 mL min^{-1}).

Electrochemical Characterization

All electrochemical tests were carried out on pelletized samples, by pressing the powder in a hydraulic uniaxial press, with a pressure ranging from 100 to 550 MPa, depending on the mixture. Pellet dimensions were 10 mm of diameter and thickness about 0.5 mm for EIS. A layer of acetylene black of negligible thickness was applied on both pellet surfaces before pressing with the final loading. EIS spectra were collected with a Biologic SP-200, in a frequency range $10^{-2} < f < 7 \times 10^7$ Hz with an AC perturbation signal of 10 mV. The temperature was controlled with a nitrogen stream in a Novocontrol temperature controller and sample holder in the range 173 < T < 453 K.

SSRCVs were performed in a polytetrafluoroethylene (PTFE) Swagelok cell, with pellet dimension of 6 mm diameter and 0.5 mm thickness. A polished, hand-scratched, sodium (Sigma-Aldrich; ACS reagent grade) foil was punched on a 5-mm disk (thickness <0.1 mm) and was used as self-reference electrode. Glassy carbon (Sigradur 180 μm thickness, purchased at HTW) was selected as working electrode. Despite emphasis in a previous publication on the importance of increasing the surface area by the addition of conductive carbon to detect reliable oxidation peaks,[13] the adoption of the latter could also perturb the system, decreasing the barrier of decomposition process kinetics.[55] Therefore, a close-to-equilibrium slow sweeping rate (20 $\mu V\ s^{-1}$) was adopted in order to allow the detection of small surface processes as described in section "Electrochemical Stability."

All the sample manipulations described in the experimental section were carried out in an Ar-filled glove box (H_2O and O_2 < 0.1 ppm).

SUPPLEMENTAL INFORMATION

Supplemental Information can be found online at https://doi.org/10.1016/j.xcrp.2020.100217.

ACKNOWLEDGMENTS

The authors acknowledge the Swiss-Norwegian Beamlines of ESRF and the Materials Science beamline of the SLS for the allocation of beamtime and excellent support with the data collection. The authors thank Prof. Hans Hagemann, Physical Chemistry Dpt. of the University of Geneva, for the use of DSC and Raman spectroscopy installations. Dr. Siobhan McKeown Walker is also deeply acknowledged for the fruitful discussions. This work was funded by the University of Geneva.

AUTHOR CONTRIBUTIONS

M.B. and F.M. conducted the experiments; M.B. and R.Č. designed the experiments. The manuscript was written through contributions of all authors. All authors have given approval to the final version of the manuscript.

DECLARATION OF INTERESTS

The authors declare no competing interests.

Received: July 3, 2020
Revised: August 14, 2020
Accepted: September 3, 2020
Published: October 7, 2020

REFERENCES

1. Amnesty International (2019). Amnesty challenges industry leaders to clean up their batteries. https://www.amnesty.org/en/latest/news/2019/03/amnesty-challenges-industry-leaders-to-clean-up-their-batteries/.

2. Armstrong, R.D., Dickinson, T., and Turner, J. (1974). The breakdown of β-alumina ceramic electrolyte. Electrochim. Acta *19*, 187–192.

3. Taylor, N.J., Stangeland-Molo, S., Haslam, C.G., Sharafi, A., Thompson, T., Wang, M., Garcia-Mendez, R., and Sakamoto, J. (2018). Demonstration of high current densities and extended cycling in the garnet $Li_7La_3Zr_2O_{12}$ solid electrolyte. J. Power Sources *396*, 314–318.

4. Pokorný, V., Štejfa, V., Fulem, M., Červinka, C., and Růžička, K. (2017). Vapor pressures and thermophysical properties of ethylene carbonate, propylene carbonate, γ-valerolactone, and γ-butyrolactone. J. Chem. Eng. Data *62*, 4174–4186.

5. Yoshida, K., Suzuki, S., Kawaji, J., Unemoto, A., and Orimo, S. (2016). Complex hydride for composite negative electrode—applicable to bulk-type all-solid-state Li-ion battery with wide temperature operation. Solid State Ion. *285*, 96–100.

6. Unemoto, A., Matsuo, M., and Orimo, S. (2014). Complex hydrides for electrochemical energy storage. Adv. Funct. Mater. *24*, 2267–2279.

7. Duchêne, L., Kühnel, R.-S., Stilp, E., Cuervo Reyes, E., Remhof, A., Hagemann, H., and Battaglia, C. (2017). A stable 3 V all-solid-state sodium-ion battery based on a *closo*-borate electrolyte. Energy Environ. Sci. *10*, 2609–2615.

8. Kim, S., Oguchi, H., Toyama, N., Sato, T., Takagi, S., Otomo, T., Arunkumar, D., Kuwata, N., Kawamura, J., and Orimo, S.I. (2019). A complex hydride lithium superionic conductor for high-energy-density all-solid-state lithium metal batteries. Nat. Commun. *10*, 1081.

9. Murgia, F., Brighi, M., and Černý, R. (2019). Room-temperature-operating Na solid-state battery with complex hydride as electrolyte. Electrochem. Commun. *106*, 106534.

10. Sadikin, Y., Schouwink, P., Brighi, M., Łodziana, Z., and Černý, R. (2017). Modified anion packing of $Na_2B_{12}H_{12}$ in close to room temperature superionic conductors. Inorg. Chem. *56*, 5006–5016.

11. Gulino, V., Brighi, M., Dematteis, E.M., Murgia, F., Nervi, C., Černý, R., and Baricco, M. (2019). Phase stability and fast ion conductivity in the hexagonal $LiBH_4$–LiBr–LiCl solid solution. Chem. Mater. *31*, 5133–5144.

12. Duchêne, L., Kühnel, R.-S., Rentsch, D., Remhof, A., Hagemann, H., and Battaglia, C. (2017). A highly stable sodium solid-state electrolyte based on a dodeca/deca-borate equimolar mixture. Chem. Commun. (Camb.) *53*, 4195–4198.

13. Brighi, M., Murgia, F., Łodziana, Z., Schouwink, P., Wołczyk, A., and Cerny, R. (2018). A mixed anion hydroborate/carba-hydroborate as a room temperature Na-ion solid electrolyte. J. Power Sources *404*, 7–12.

14. Wiersema, R.J., and Hawthorne, M.F. (1973). Electrochemistry and boron-11 nuclear magnetic resonance spectra of monocarbon carboranes. Inorg. Chem. *12*, 785–788.

15. Muetterties, E.L., Balthis, J.H., Chia, Y.T., Knoth, W.H., and Miller, H.C. (1964). Chemistry of boranes. VIII. Salts and acids of $B_{10}H_{10}^{-2}$ and $B_{12}H_{12}^{-2}$. Inorg. Chem. *3*, 444–451.

16. He, L., Li, H.W., and Akiba, E. (2015). Thermal decomposition of anhydrous alkali metal dodecaborates $M_2B_{12}H_{12}$ (M = Li, Na, K). Energies *8*, 12429–12438.

17. Verdal, N., Her, J.-H., Stavila, V., Soloninin, A.V., Babanova, O.A., Skripov, A.V., Udovic, T.J., and Rush, J.J. (2014). Complex high-temperature phase transitions in $Li_2B_{12}H_{12}$ and $Na_2B_{12}H_{12}$. J. Solid State Chem. *212*, 81–91.

18. Skripov, A.V., Babanova, O.A., Soloninin, A.V., Stavila, V., Verdal, N., Udovic, T.J., and Rush, J.J. (2013). Nuclear magnetic resonance study of atomic motion in $A_2B_{12}H_{12}$ (A = Na, K, Rb, Cs): anion reorientations and Na^+ mobility. J. Phys. Chem. C *117*, 25961–25968.

19. Kweon, K.E., Varley, J.B., Shea, P., Adelstein, N., Mehta, P., Heo, T.W., Udovic, T.J., Stavila, V., and Wood, B.C. (2017). Structural, chemical, and dynamical frustration: origins of superionic conductivity in *closo*-borate solid electrolytes. Chem. Mater. *29*, 9142–9153.

20. Capillas, C., Perez-Mato, J.M., and Aroyo, M.I. (2007). Maximal symmetry transition paths for reconstructive phase transitions. J. Phys.: Condens. Matter *19*, 275203.

21. Keen, D.A. (2002). Disordering phenomena in superionic conductors. J. Phys. Condens. Matter *14*, R819–R857.

22. Tang, W.S., Yoshida, K., Soloninin, A.V., Skoryunov, R.V., Babanova, O.A., Skripov, A.V., Dimitrievska, M., Stavila, V., Orimo, S., and Udovic, T.J. (2016). Stabilizing superionic-conducting structures via mixed-anion solid solutions of monocarba- closo -borate salts. ACS Energy Lett. *1*, 659–664.

23. Skripov, A.V., Skoryunov, R.V., Soloninin, A.V., Babanova, O.A., Tang, W.S., Stavila, V., and Udovic, T.J. (2015). Anion reorientations and cation diffusion in $LiCB_{11}H_{12}$ and $NaCB_{11}H_{12}$: ^1H, ^7Li, and ^{23}Na NMR studies. J. Phys. Chem. C *119*, 26912–26918.

24. Udovic, T.J., Matsuo, M., Tang, W.S., Wu, H., Stavila, V., Soloninin, A.V., Skoryunov, R.V., Babanova, O.A., Skripov, A.V., Rush, J.J., et al. (2014). Exceptional superionic conductivity in disordered sodium decahydro-closo-decaborate. Adv. Mater. *26*, 7622–7626.

25. Tang, W.S., Matsuo, M., Wu, H., Stavila, V., Zhou, W., Talin, A.A., Soloninin, A.V., Skoryunov, R.V., Babanova, O.A., and Skripov, A.V. (2016). Liquid-like ionic conduction in solid lithium and sodium monocarba- closo -decaborates near or at room temperature. Adv. Energy Mater. *6*, 1502237.

26. Yoshiasa, A., Kanamaru, F., and Koto, K. (1988). Local structure of the superionic conducting α-AgI type $AgI_{1-x}Br_x$ solid-solution. Solid State Ion. *27*, 275–283.

27. Reuter, B., and Hardel, K. (1965). Silbersulfidbromid Ag_3SBr und silbersulfidjodid Ag_3SJ. II. Die kristallstrukturen von Ag_3SBr, β- und α-Ag_3SJ. Z. Anorg. Allg. Chem. *340*, 168–180.

28. Payandeh, S., Asakura, R., Avramidou, P., Rentsch, D., Łodziana, Z., Černý, R., Remhof, A., and Battaglia, C. (2020). Nido-borate/*Closo*-borate mixed-anion electrolytes for all-solid-state batteries. Chem. Mater. *32*, 1101–1110.

29. Lee, W.K., Liu, J.F., and Nowick, A.S. (1991). Limiting behavior of ac conductivity in ionically conducting crystals and glasses: A new universality. Phys. Rev. Lett. *67*, 1559–1561.

30. Duchêne, L., Lunghammer, S., Burankova, T., Liao, W.-C., Embs, J.P., Copéret, C., Wilkening, H.M.R., Remhof, A., Hagemann, H., and Battaglia, C. (2019). Ionic conduction mechanism in the $Na_2(B_{12}H_{12})_{0.5}(B_{10}H_{10})_{0.5}$*closo*-borate solid-state electrolyte: interplay of disorder and ion-ion interactions. Chem. Mater. *31*, 3449–3460.

31. Irvine, J.T.S., Sinclair, D.C., and West, A.R. (1990). Electroceramics: characterization by impedance spectroscopy. Adv. Mater. *2*, 132–138.

32. Ngai, K.L., Jonscher, A.K., and White, C.T. (1979). On the origin of the universal dielectric response in condensed matter. Nature *277*, 185–189.

33. Trachenko, K., and Brazhkin, V.V. (2011). Heat capacity at the glass transition. Phys. Rev. B *83*, 014201.

34. Varley, J.B., Kweon, K., Mehta, P., Shea, P., Heo, T.W., Udovic, T.J., Stavila, V., and Wood, B.C. (2017). Understanding ionic conductivity trends in polyborane solid electrolytes from ab initio molecular dynamics. ACS Energy Lett. *2*, 250–255.

35. Ngai, K.L. (1998). Meyer–Neldel rule and anti Meyer–Neldel rule of ionic conductivity: conclusions from the coupling model. Solid State Ion. *105*, 231–235.

36. Yelon, A., Movaghar, B., and Branz, H.M. (1992). Origin and consequences of the compensation (Meyer-Neldel) law. Phys. Rev. B Condens. Matter *46*, 12244–12250.

37. Kraft, M.A., Culver, S.P., Calderon, M., Böcher, F., Krauskopf, T., Senyshyn, A., Dietrich, C., Zevalkink, A., Janek, J., and Zeier, W.G. (2017). Influence of lattice polarizability on the ionic conductivity in the lithium superionic argyrodites Li_6PS_5X (X = Cl, Br, I). J. Am. Chem. Soc. *139*, 10909–10918.

38. Culver, S.P., Koerver, R., Krauskopf, T., and Zeier, W.G. (2018). Designing ionic conductors: the interplay between structural phenomena and interfaces in thiophosphate-based solid-state batteries. Chem. Mater. *30*, 4179–4192.

39. Hazen, R.M., and Yang, H. (1997). Increased compressibility of pseudobrookite-type $MgTi_2O_5$ caused by cation disorder. Science *277*, 1965–1967.

40. Kamaya, N., Homma, K., Yamakawa, Y., Hirayama, M., Kanno, R., Yonemura, M., Kamiyama, T., Kato, Y., Hama, S., Kawamoto, K., and Mitsui, A. (2011). A lithium superionic conductor. Nat. Mater. *10*, 682–686.

41. Boulineau, S., Courty, M., Tarascon, J.M., and Viallet, V. (2012). Mechanochemical synthesis of Li-argyrodite Li6PS5X (X = Cl, Br, I) as sulfur-based solid electrolytes for all solid state batteries application. Solid State Ion. *221*, 1–5.

42. Asakura, R., Duchêne, L., Kühnel, R.-S., Remhof, A., Hagemann, H., and Battaglia, C. (2019). Electrochemical oxidative stability of hydroborate-based solid-state electrolytes. ACS Appl. Energy Mater. *2*, 6924–6930.

43. Middaugh, R.L., and Farha, F., Jr. (1966). Kinetics of electrochemical oxidative coupling of decahydroclovodecaborate(2–) in acetonitrile. J. Am. Chem. Soc. *88*, 4147–4149.

44. Tutusaus, O., Mohtadi, R., Arthur, T.S., Mizuno, F., Nelson, E.G., and Sevryugina, Y.V. (2015). An efficient halogen-free electrolyte for use in rechargeable magnesium batteries. Angew. Chem. Int. Ed. Engl. *54*, 7900–7904.

45. Reed, C.A. (1998). Carboranes: a new class of weakly coordinating anions for strong electrophiles, oxidants, and superacids. Acc. Chem. Res. *31*, 133–139.

46. Schleyer, P.R., and Najafian, K. (1998). Stability and three-dimensional aromaticity of closo-monocarbaborane anions, CB(n)(-)(1)H(n)(-), and closo-dicarboranes, C(2)B(n)(-)(2)H(n). Inorg. Chem. *37*, 3454–3470.

47. Aihara, J. (1978). Three-dimensional aromaticity of polyhedral boranes. J. Am. Chem. Soc. *100*, 3339–3342.

48. Grimes, R.N. (2016). Carboranes, Third Edition (Academic).

49. Moury, R., Łodziana, Z., Remhof, A., Duchêne, L., Roedern, E., Gigante, A., and Hagemann, H. (2019). Pressure-induced phase transitions in $Na_2B_{12}H_{12}$, structural investigation on a candidate for solid-state electrolyte. Acta Crystallogr. Sect. B Struct. Sci. Cryst. Eng. Mater. *75*, 406–413.

50. Orobengoa, D., Capillas, C., Aroyo, M.I., and Perez-Mato, J.M. (2009). *AMPLIMODES*: symmetry-mode analysis on the Bilbao Crystallographic Server. J. Appl. Cryst. *42*, 820–833.

51. Perez-Mato, J.M., Orobengoa, D., and Aroyo, M.I. (2010). Mode crystallography of distorted structures. Acta Crystallogr. A *66*, 558–590.

52. Favre-Nicolin, V., and Cerný, R. (2002). FOX, 'free objects for crystallography': a modular approach to *ab initio* structure determination from powder diffraction. J. Appl. Cryst. *35*, 734–743.

53. Coelho, A.A. (2000). Whole-profile structure solution from powder diffraction data using simulated annealing. J. Appl. Cryst. *33*, 899–908.

54. Momma, K., and Izumi, F. (2011). *VESTA 3* for three-dimensional visualization of crystal, volumetric and morphology data. J. Appl. Cryst. *44*, 1272–1276.

55. Zhang, W., Leichtweiß, T., Culver, S.P., Koerver, R., Das, D., Weber, D.A., Zeier, W.G., and Janek, J. (2017). The detrimental effects of carbon additives in $Li_{10}GeP_2S_{12}$-based solid-state batteries. ACS Appl. Mater. Interfaces *9*, 35888–35896.

Cell Reports Physical Science, Volume *1*

Supplemental Information

Closo-Hydroborate Sodium Salts as an Emerging Class of Room-Temperature Solid Electrolytes

Matteo Brighi, Fabrizio Murgia, and Radovan Černý

Note S1

Structural analysis of the lattice distortion for single anion *closo*-hydroborates and *closo*-carbahydroborates across the phase transition

$NaCB_9H_{10}$

T=240 K $P2_1/c \rightarrow Pna2_1$

Transformation matrix (to allow group-subgroup relation, an equivalent structure was created with the s.g. $P2_1$; transformation index *i*=4)

$$(P,p) = \begin{pmatrix} 1 & 0 & -2 & 0 \\ -1 & 0 & 0 & 0 \\ 0 & 1 & 0 & 0.2838 \end{pmatrix}$$

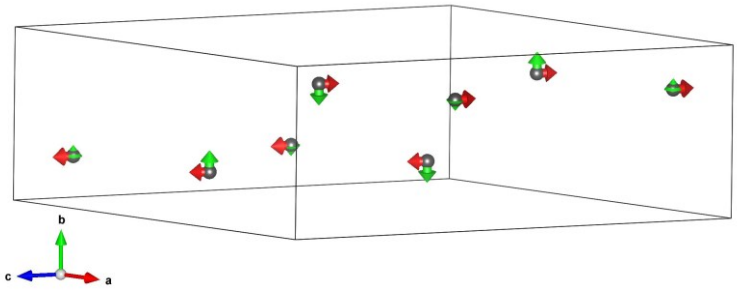

The symmetry mode analysis consisted of three modes:

GM1 and GM2 at K=(0, 0, 0) and

S1S2 at K=(1/2, 1/2, 0)
The degree of lattice distortion amount to S = 0.0078

T=310 K $Pna2_1 \rightarrow P6_3/mmc$

Transformation matrix; transformation index *i*=12)

$$(P,p) = \begin{pmatrix} 0 & 1 & 1 & 0.2162 \\ 0 & -1 & 1 & -0.2838 \\ 1 & 0 & 0 & 1/2 \end{pmatrix}$$

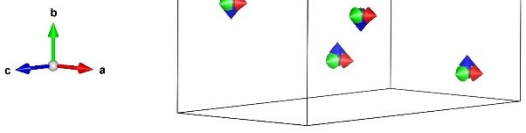

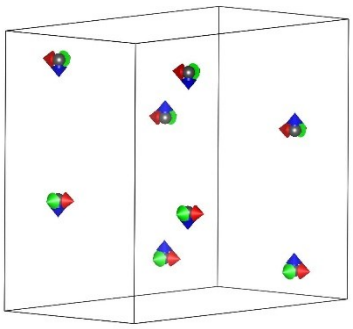

The symmetry mode analysis consisted of three modes:

GM5+ and GM6- at K=(0,0,0) and
M2- at K=(1/2, 0, 0)
The degree of lattice distortion amount to S = 0.0649

$Na_2B_{10}H_{10}$

T=360 K $P2_1/c \rightarrow Fm\text{-}3m$

Transformation matrix (to allow group-subgroup relation, an equivalent structure was created with the s.g. *Fm*-3; transformation index *i*=48)

$$(P,p) = \begin{pmatrix} 1/2 & -1 & -1/2 & 1/4 \\ -1/2 & -1 & 1/2 & 0 \\ 0 & 0 & -1 & -1/4 \end{pmatrix}$$

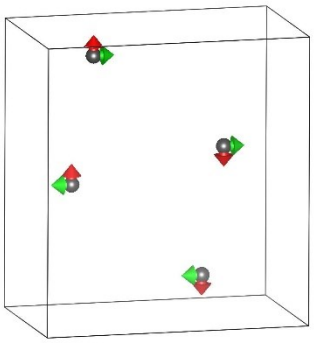

The symmetry mode analysis consisted of three modes:

SM2 and SM3 at K=(1/2, 1/2, 0) and
X5- at K=(0, 1, 0)
The degree of lattice distortion amount to S = 0.0312

$NaCB_{11}H_{12}$

T=360 K $Pca2_1 \rightarrow Fm\text{-}3m$

Transformation matrix (to allow group-subgroup relation, an equivalent structure was created with the s.g. *Fm*-3; transformation index *i*=48)

$$(P,p) = \begin{pmatrix} 0 & 1 & 0 & 1/4 \\ -1 & 0 & 0 & -1/2 \\ 0 & 0 & 1 & 0.0204 \end{pmatrix}$$

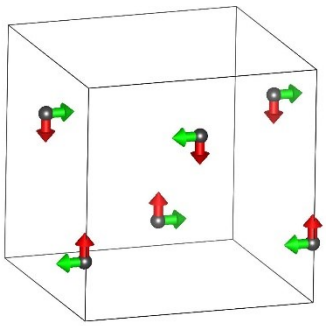

The symmetry mode analysis consisted of three modes:

GM4- (δ=0) at K=(0, 0, 0) and
X3- and X5- at K=(0, 1, 0)
The degree of lattice distortion amount to S = 0.0185

$Na_2B_{12}H_{12}$

Two transitions happen at temperatures close to each other:[1]

T=513 K $P2_1/n \rightarrow Pm\text{-}3n$

T=519 K $P2_1/n \rightarrow Fm\text{-}3m$

Since it is impossible to obtain a group/subgroup relation for the first transition and because the second transition involves only unit cell deformation, analysis of the strain with the utility “STRAIN” of the Bilbao Crystallographic Server was used.

In the first case, a monoclinic cell (a=7.0306 Å; b=10.6540 Å; c=7.0090 Å; β=94.676°) transforms to a *bcc* cell (a=8.0547 Å) with a finite Lagrangian strain tensor:

$$\begin{pmatrix} -0.119056 & 1 & -0.030959 \\ 0 & 0.374778 & 0 \\ -0.030959 & 0 & -0.121396 \end{pmatrix}$$ from which S amounts to 0.13796

For the second transition, being the monoclinic cell a deformed *ccp* cell, the deformation is minimal. In this case the cells parameters used were a=7.0306 Å; b=7.009 Å; c=10.654 Å; γ=94.676° for the monoclinic cell and a=10.5288 Å for the cubic cell. The finite Lagrangian strain tensor is:

$$\begin{pmatrix} -0.054104 & -0.036238 & 0 \\ -0.036238 & -0.056842 & 0 \\ 0 & 0 & 0.011966 \end{pmatrix}$$ from which S amounts to 0.0315

Since $Na_2B_{12}H_{12}$ is stable at *rt* as *ccp* anion packing, while at high temperature the *bcc* becomes the stable anion packing, one could state that an intermediate, metastable, state is obtained by means of *ccp* structure, giving the whole transition path as:

P2_1/*n* → *Fm*-3*m* → *Pm*-3*n*

If this was the case, the second step of the distortion will result in a finite Lagrangian strain tensor:

$$\begin{pmatrix} 0.082541 & 0 & 0 \\ 0 & 0.082541 & 0 \\ 0 & 0 & -0.20873 \end{pmatrix}$$ from which S amounts to 0.07972

The whole process will give a total degree of lattice distortion of S=0.11122

X-ray Powder Diffraction

Compound	s.g. (*rt*)	T_t (K)	s.g. (*ht*)	σ_{Na} (mS cm^{-1}) at $T>T_t$
$NaCB_9H_{10}$	$Pna2_1$	310	$P31c$	39 (T=317 K)
$Na_2B_{10}H_{10}$	$P2_1/c$	360	Fm-$3m$	119 (T=383 K)
$NaCB_{11}H_{12}$	$Pca2_1$	376	Fm-$3m$	7 (T=384 K)
$Na_2B_{12}H_{12}$	$P2_1/n$	529	Pm-$3n$/Im-$3m$	82 (T=543 K)

Table S1 Polymorphic evolution scheme of *closo* and carba*closo*-hydroborates with the phase transition temperature and the value of Na^+ conductivity above it.

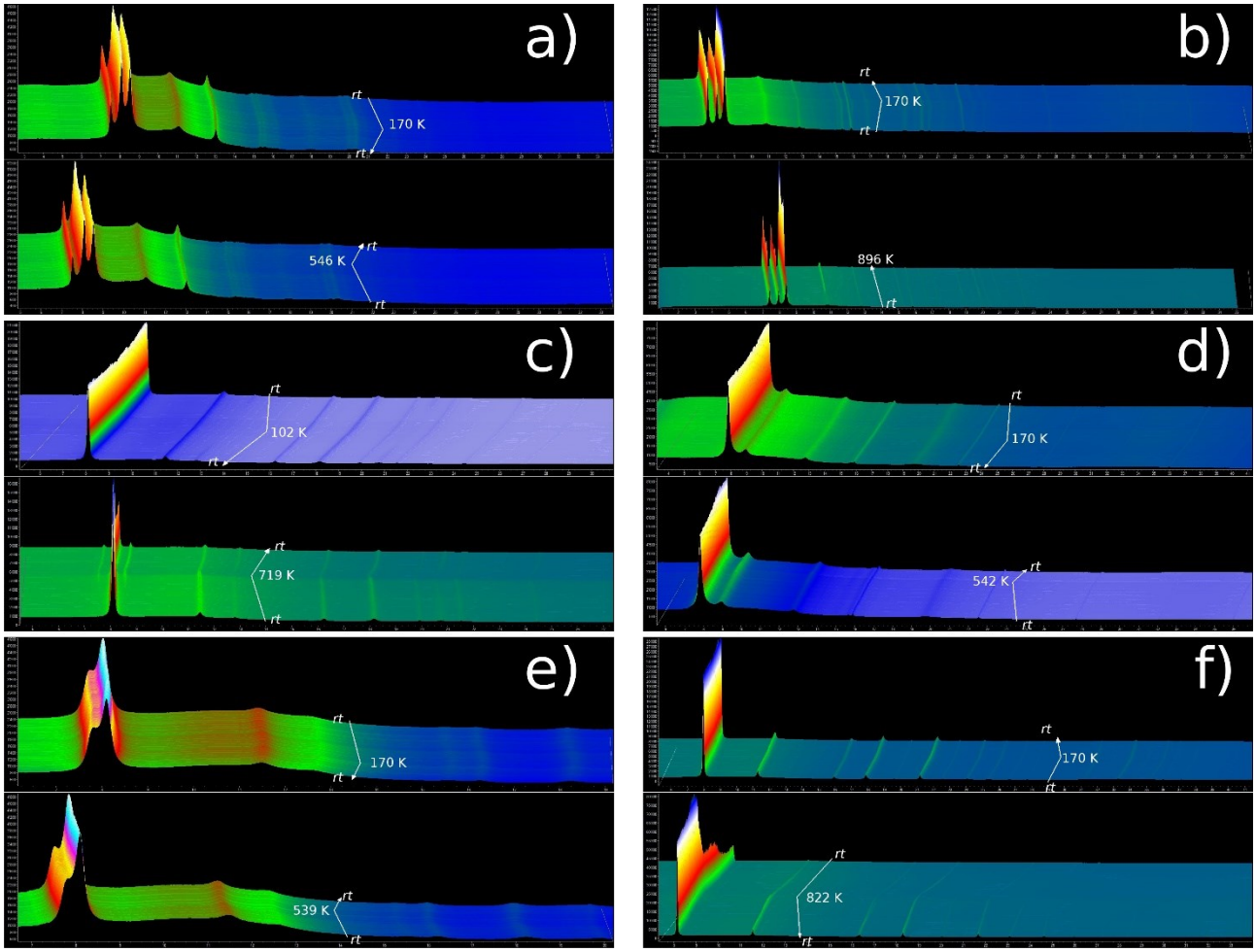

Figure S1 Synchrotron XRD *in situ* temperature ramps of mixed-anion compounds collected at SNBL (ESRF) with a wavelength of λ=0.7794 Å. Figures show: a) [CB_9-B_{10}]; b) [CB_9-CB_{11}]; c) [CB_9-B_{12}]; d) [B_{10}-CB_{11}]; e) [B_{10}-B_{12}]; and f) [CB_{11}-B_{12}]. The viewing angle is different for each figure and subfigure to optimize the observation of weak reflections.

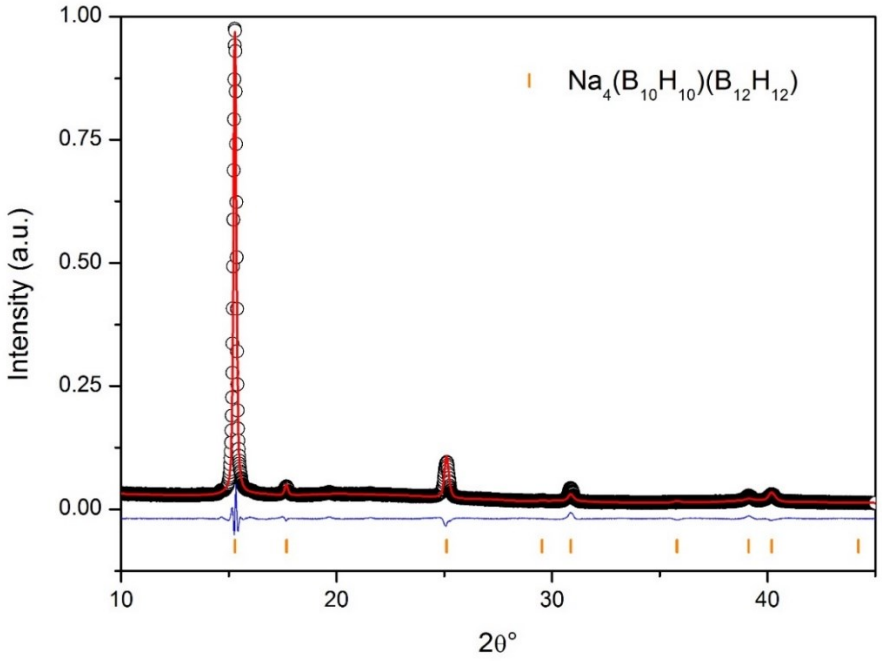

Figure S2 Rietveld plot for $Na_4(B_{10}H_{10})(B_{12}H_{12})$ measured with laboratory diffractometer. Data were collected at T=298 K, $\lambda=Cu_{K\alpha1}$, $R_{wp(bkg.corr.)}=13.34$; $R_{Bragg}=2.94$; $\chi^2=13.69$

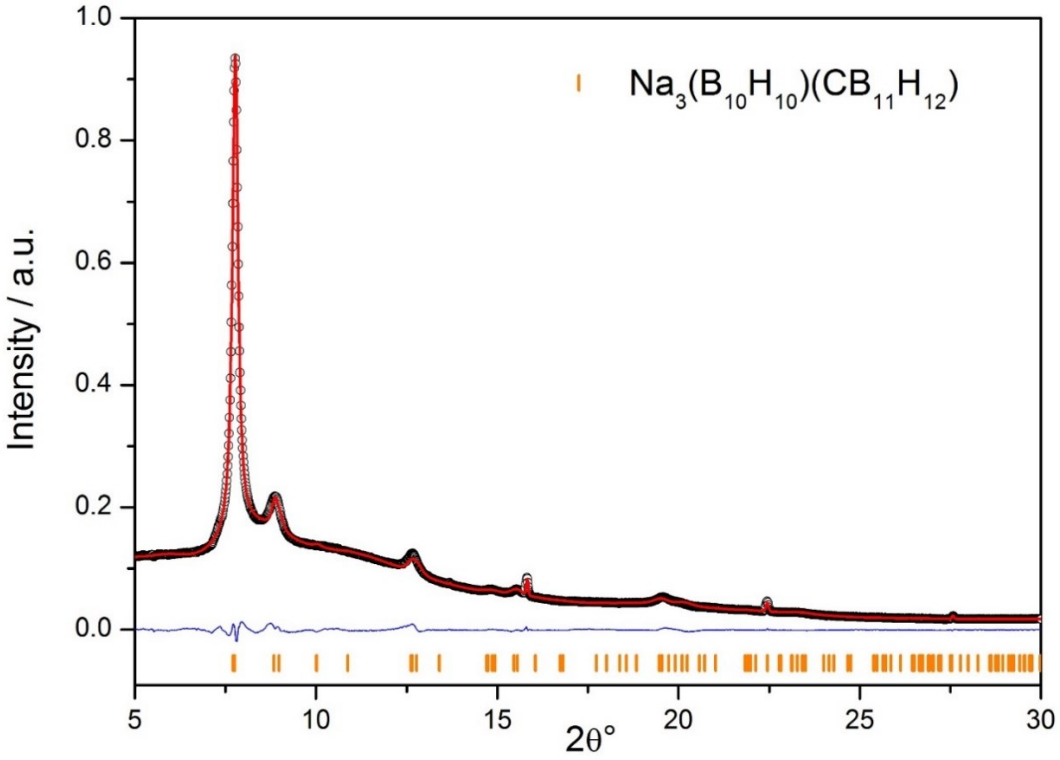

Figure S3 Rietveld plot for $Na_3(B_{10}H_{10})(CB_{11}H_{12})$ measured at SNBL, ESRF. Data were collected at T=494 K, $\lambda=0.7794$ Å, $R_{wp(bkg.corr.)}=8.39$; $R_{Bragg}=0.31$; $\chi^2=2643$

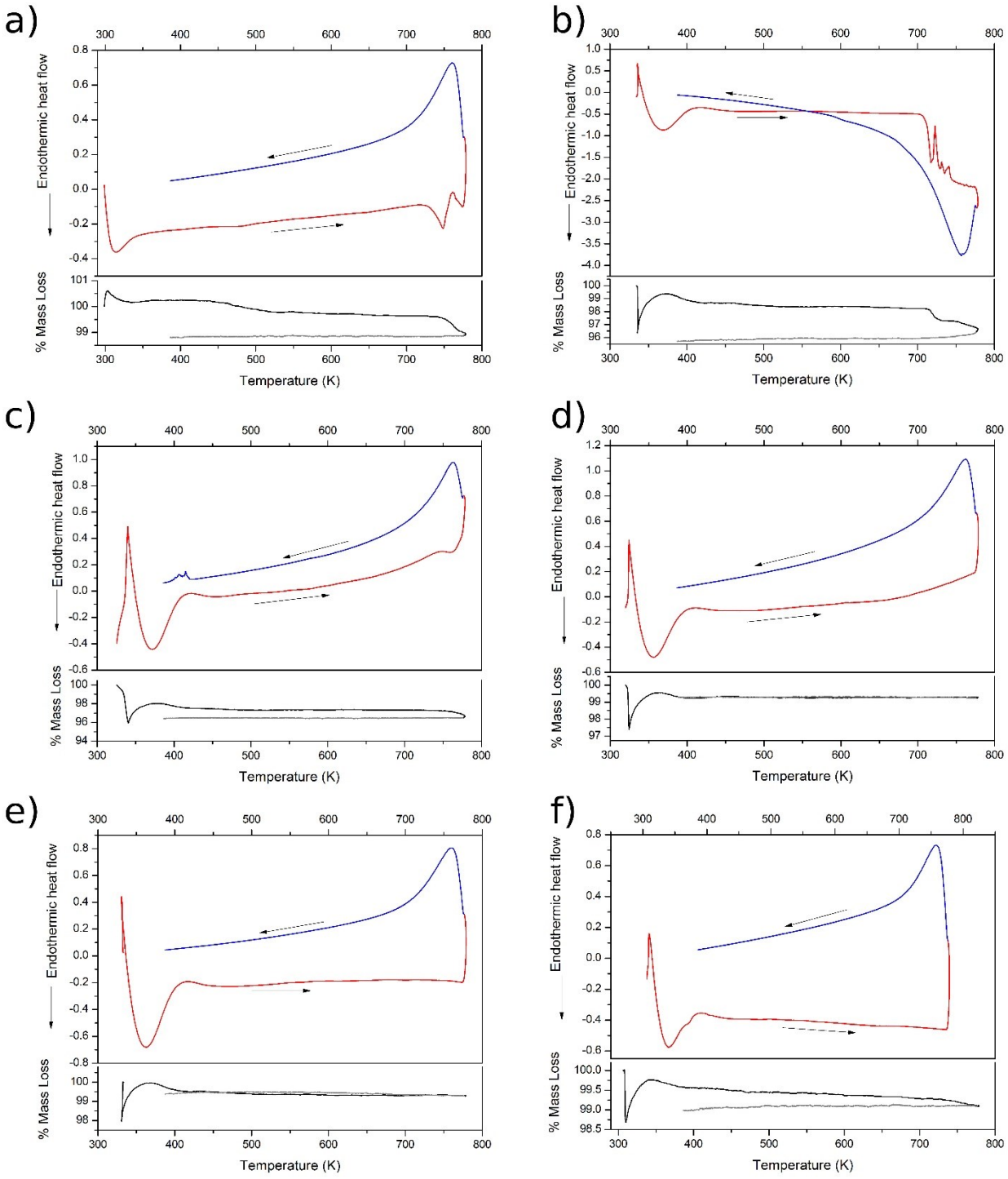

Figure S4 DSC/TG performed at physical chemistry department of University of Geneva (group of prof. Hans Hagemann). Figures show: a) [CB_9-B_{10}]; b) [CB_9-CB_{11}]; c) [CB_9-B_{12}]; d) [B_{10}-CB_{11}]; e) [B_{10}-B_{12}]; and f) [CB_{11}-B_{12}]

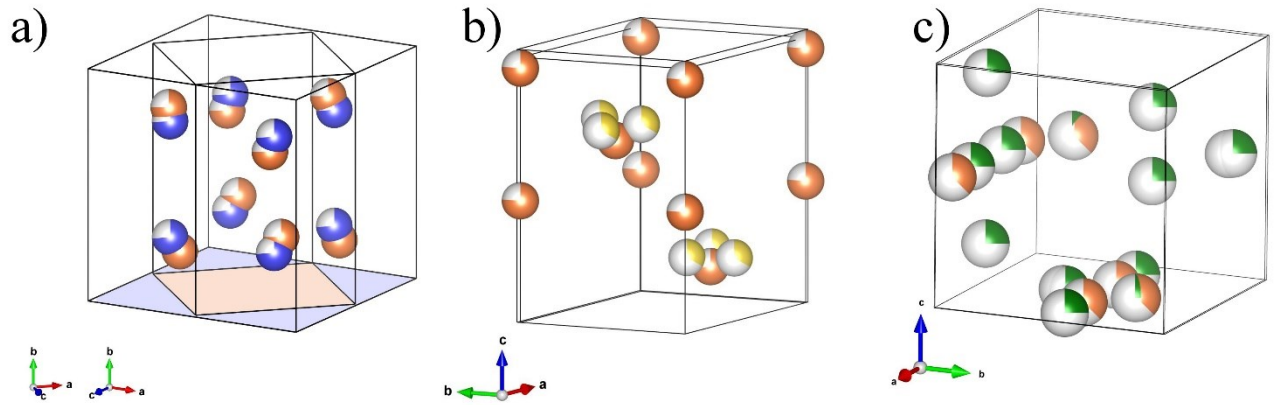

Figure S5 Comparisons of Na distributions between related structures of equivalent packing type: a) *ccp*-type with blue and orange spheres referring to [B_{10}-CB_{11}] and [B_{10}-B_{12}] respectively; b) *hcp*-type with orange and yellow spheres referring to [CB_9-B_{10}] and [CB_9-CB_{11}] respectively; c) *bcc*-type with orange and green spheres referring to [CB_9-B_{12}] and [CB_{11}-B_{12}] respectively.

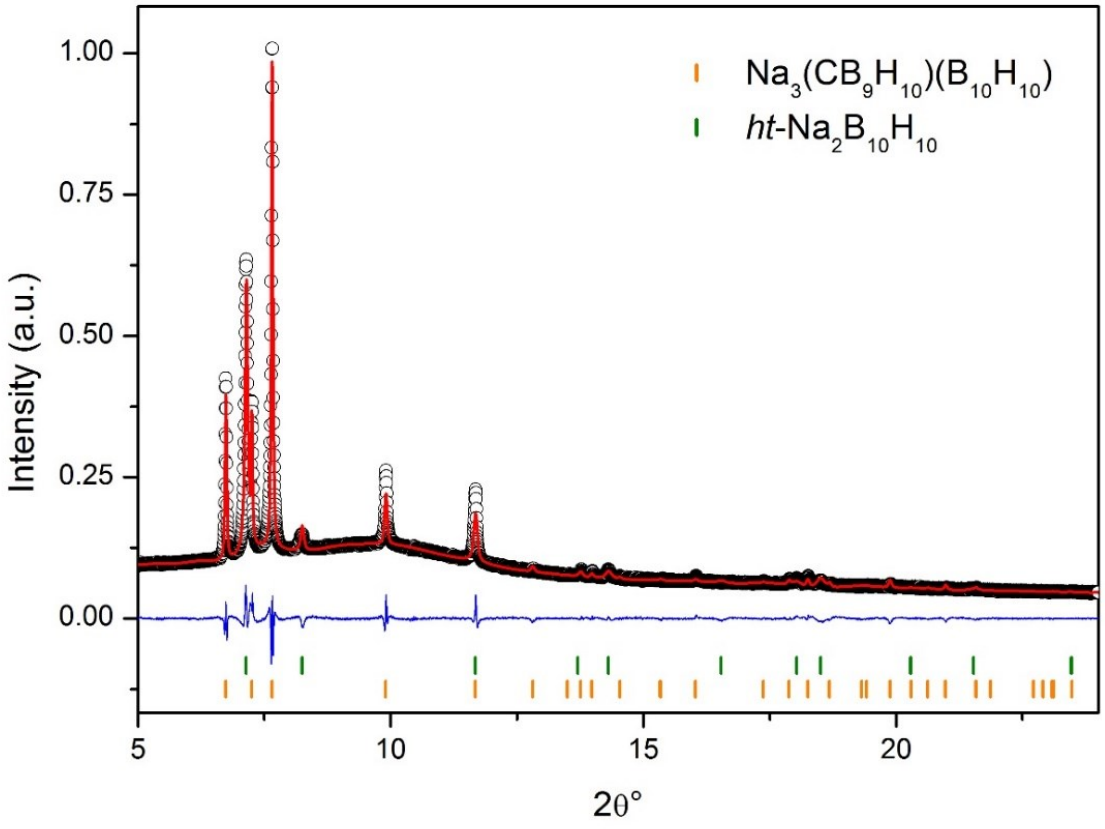

Figure S6 Rietveld plot for $Na_3(CB_9H_{10})(B_{10}H_{10})$ measured at MS-beamline SLS, PSI. Data were collected at T=500 K, λ=0.70952 Å, $R_{wp(bkg.corr.)}$=20.10; R_{Bragg}=2.53; χ^2=2.84

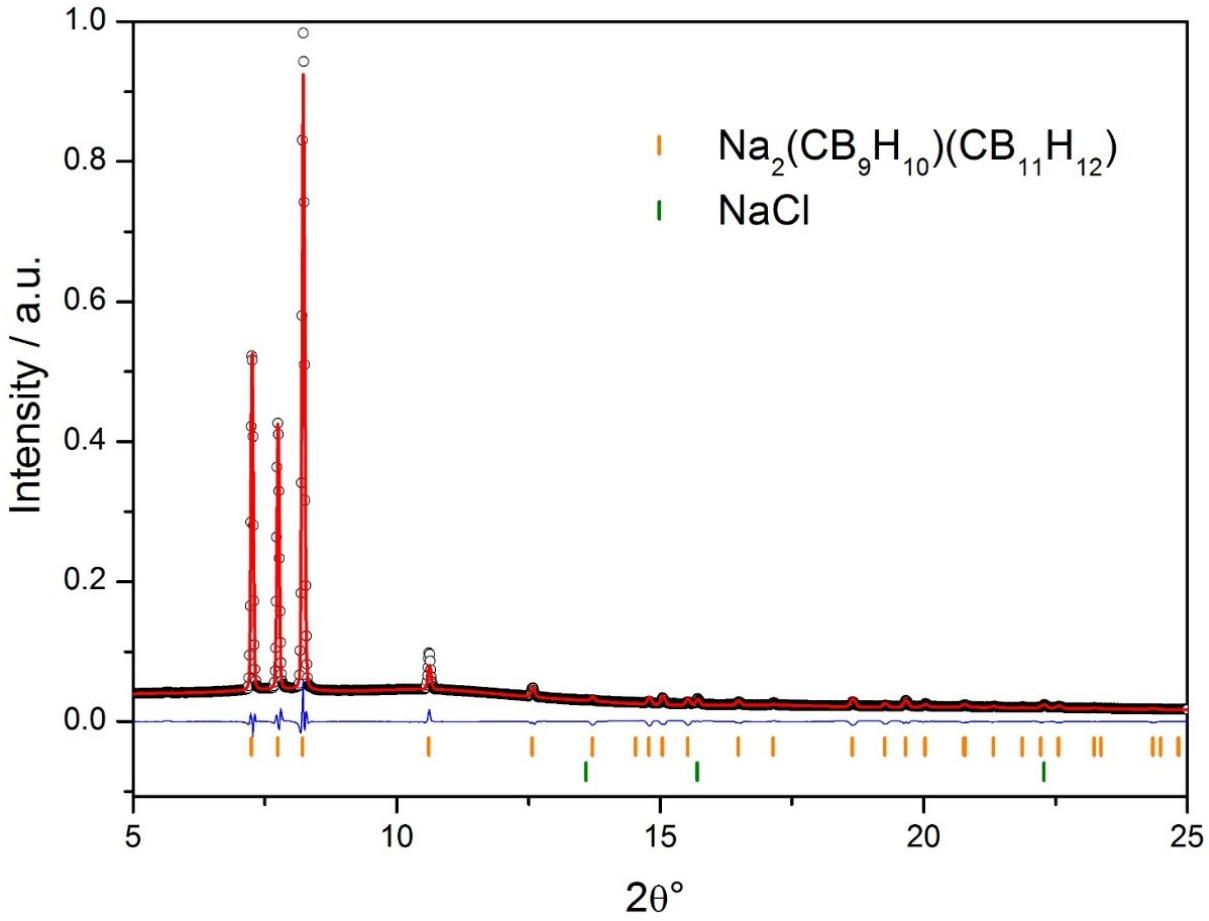

Figure S7 Rietveld plot for $Na_2(CB_9H_{10})(CB_{11}H_{12})$ measured at SNBL, ESRF. Data were collected at T=364 K, λ=0.7794 Å, $R_{wp(bkg.corr.)}$=8.25; R_{Bragg}=0.34; χ^2=410

	CB_9	B_{10}	CB_{11}	B_{12}
CB_9	207.8*	225.5	236.2	273.4
B_{10}	214.35# (Δ=-11.15)	220.9*	241.2	249.8
CB_{11}	222.70# (Δ=-13.50)	229.25# (Δ=-11.95)	237.6*	249.3
B_{12}	234.70# (Δ=-38.70)	241.25# (Δ=-8.55)	249.6# (Δ=0.3)	261.6*

Table S2 Volume/formula unit (Å^3) for the six mixed-anion compounds and the respective single anion, obtained by dividing the experimental unit cell volume by the number of anions in the cell. * refers to the *rt* polymorph cell volume, while # represents values obtained as an average of the single anion volumes (Δ represents the variation with respect to the single anion's volume).

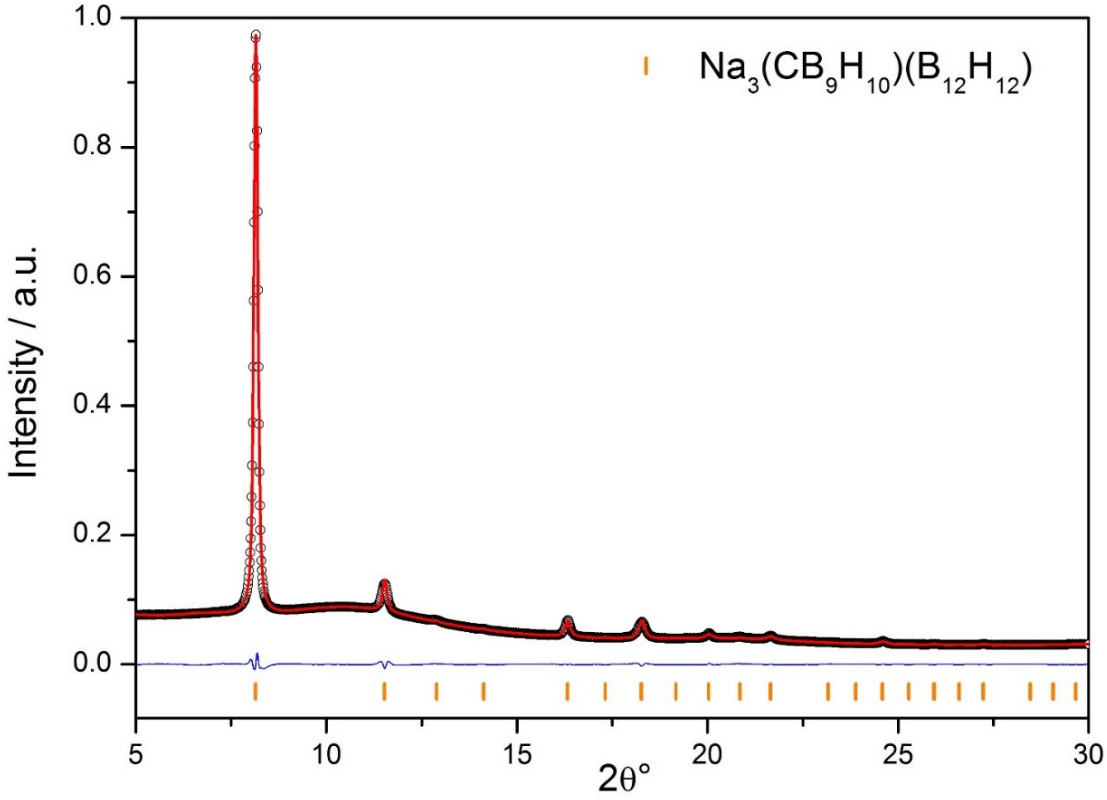

Figure S8 Rietveld plot for $Na_3(CB_9H_{10})(B_{12}H_{12})$ measured at SNBL, ESRF. Data were collected at T=430 K, λ=0.7794 Å, $R_{wp(bkg.corr.)}$=5.35; R_{Bragg}=0.07; χ^2=1875

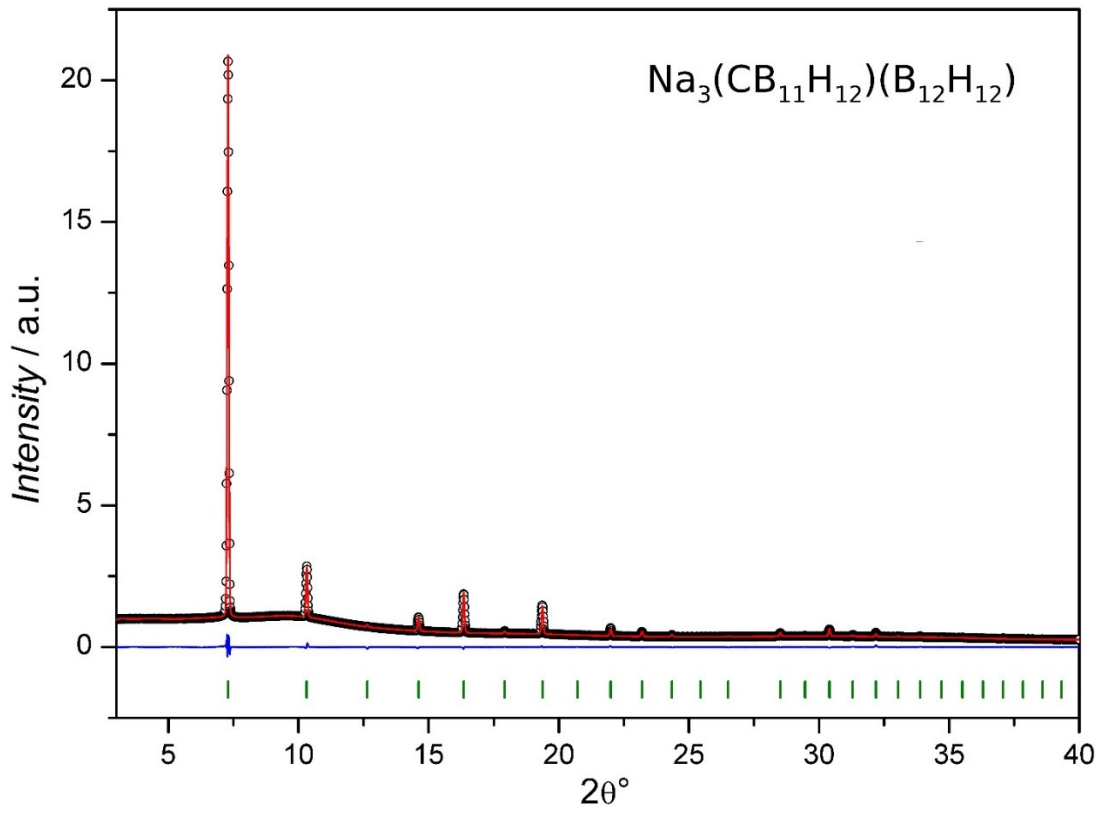

Figure S9 Rietveld plot for $Na_3(CB_{11}H_{12})(B_{12}H_{12})$ measured at SNBL, ESRF. Data were collected at T=298 K, λ=0.7143 Å, $R_{wp(bkg.corr.)}$=9.53; R_{Bragg}=0.26; χ^2=2076

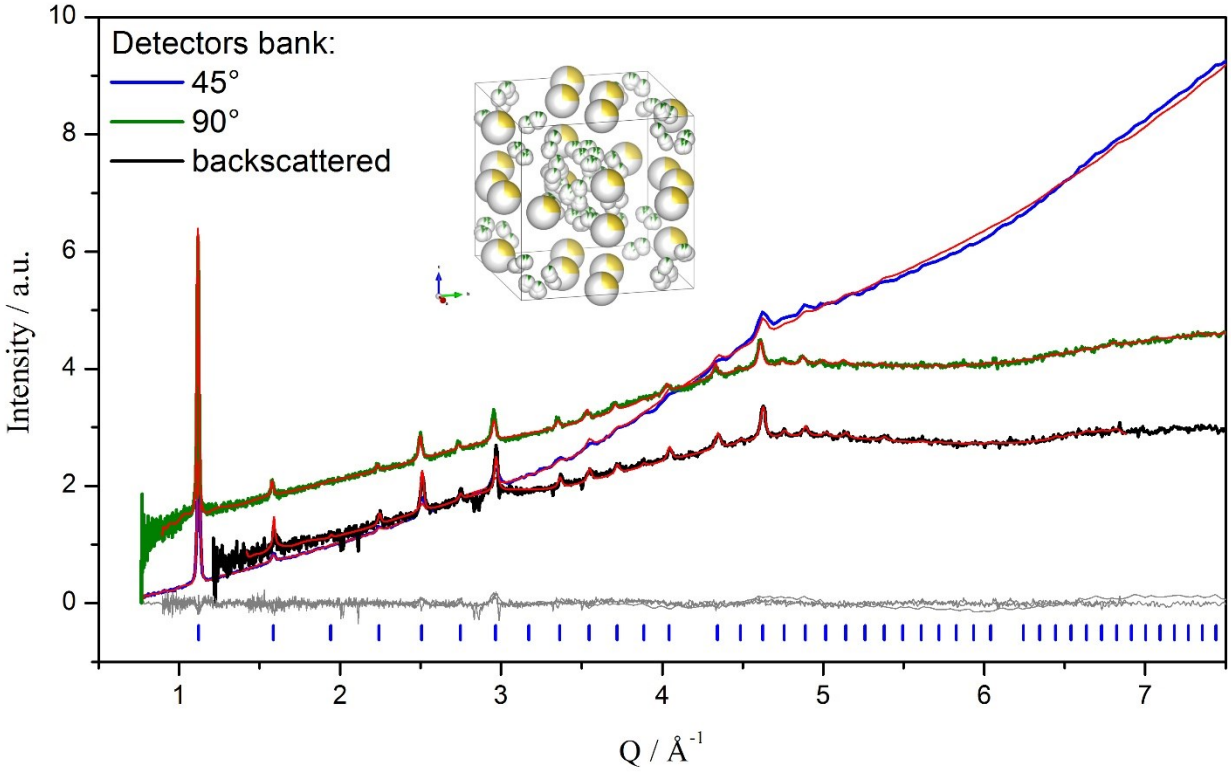

Figure S10 Rietveld plot for the *rt* TOF neutron diffraction *converges* ($R_{wp;\ bkg.\ corr.}$*=26.8,* χ^2*=397)*. X-axis in Q (Å-1). Data collected at MLF (J-PARC) with Q_{max}=107.79 Å-1. The inset shows the *I*23 model, green and yellow spheres represent boron and sodium atoms, H and D were omitted for clarity.

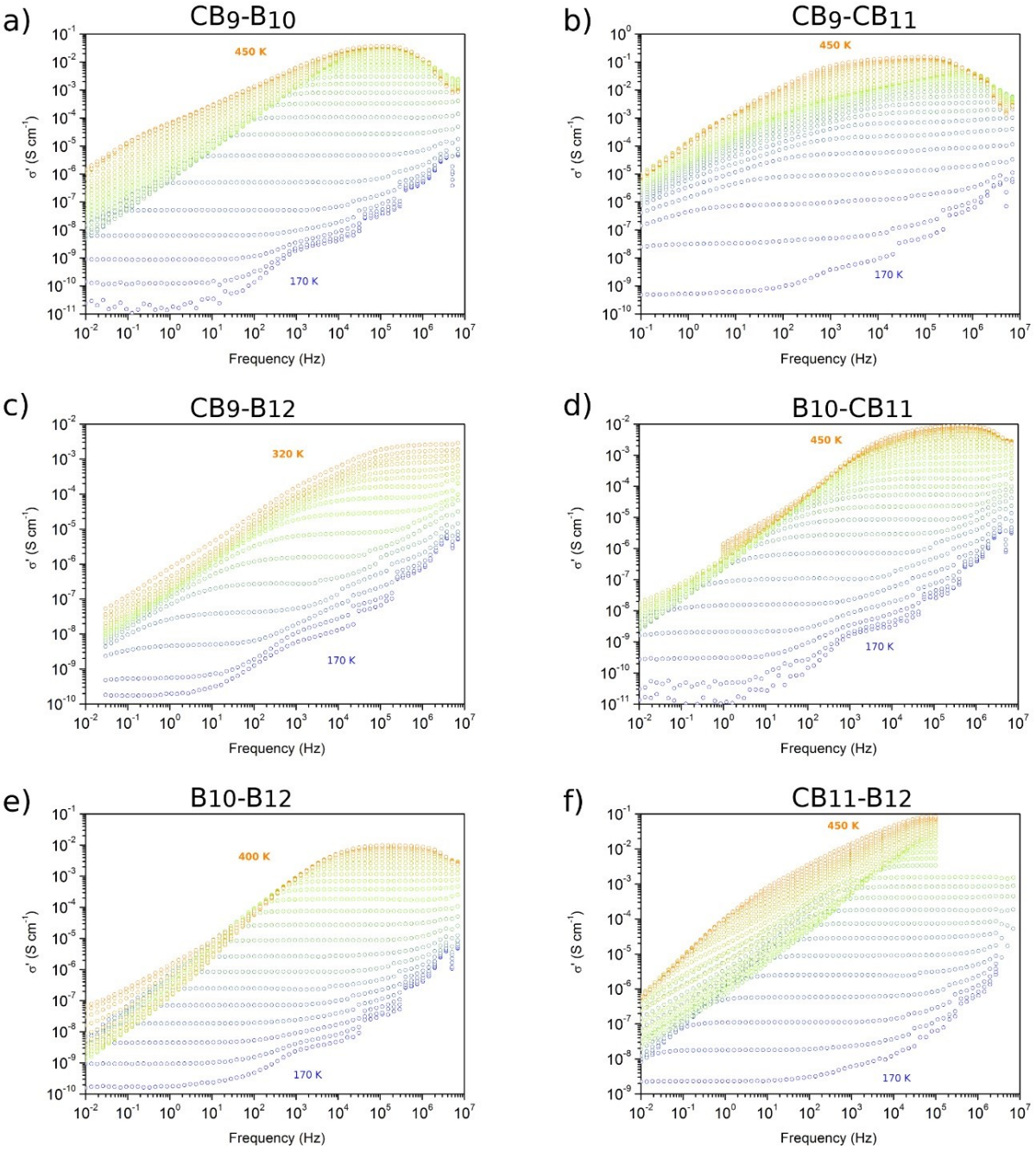

Figure S11 Real part of Na-conductivity as function of frequency.

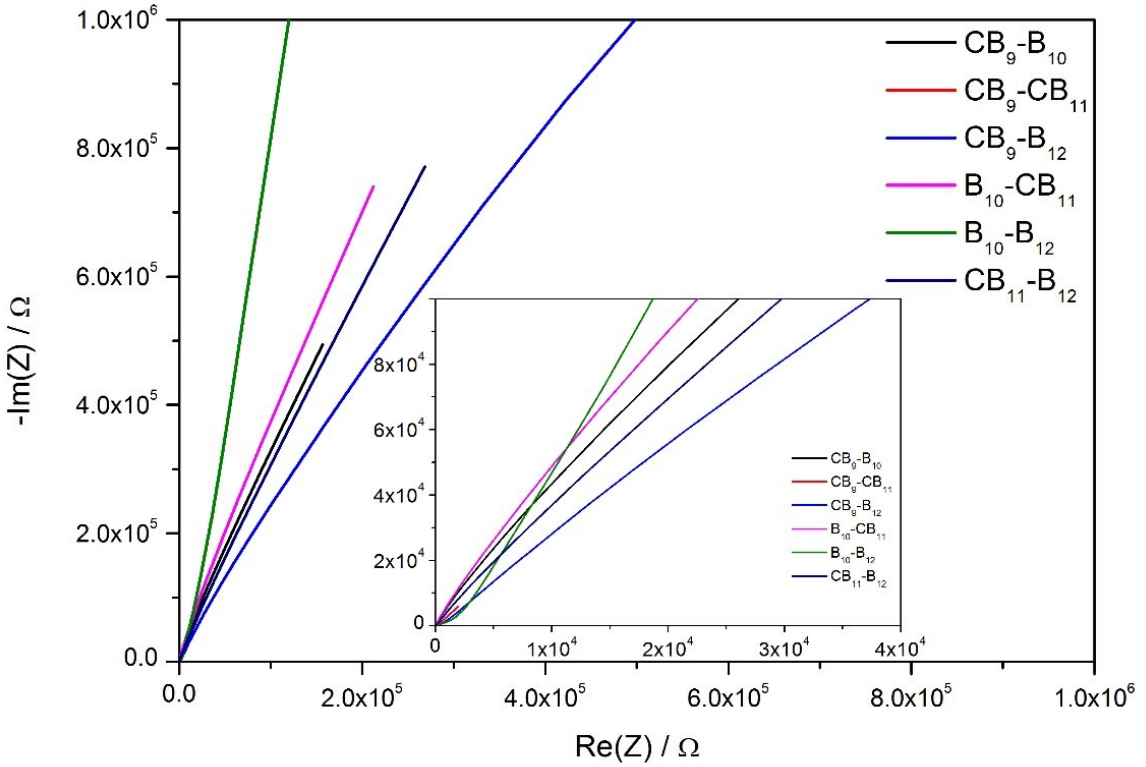

Figure S12 EIS spectra for the six mixtures obtained at 300 K. The nearly linear dispersion is associated to the polarization at the electrodes surfaces (details in Table S3)

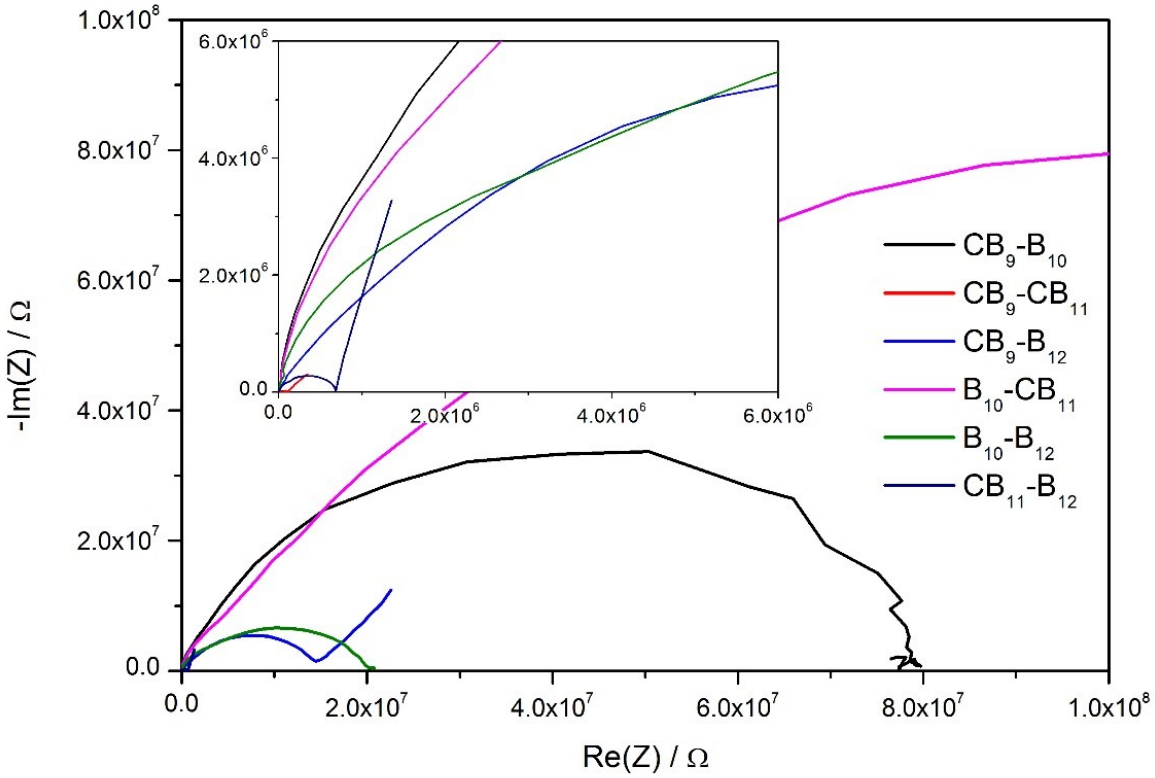

Figure S13 EIS spectra for the six mixtures obtained at 190 K. All equivalent circuits used for the fit are listed in Table S3)

9-10	Equivalent Circuit	Fitted frequency range (Hz)	χ^2
T=190 K	$(R_1Q_1)(R_2Q_2)$	$2.24 – 8.13 \times 10^4$	2×10^{-4}
	Circuit Element	Value	Error %
	R_1	2.61×10^6	12.98
	Q_1	5.36×10^{-11}	13.65
	n_1	1	2.00
	R_2	7.63×10^7	0.89
	Q_2	5.76×10^{-11}	3.74
	n_2	9.32×10^{-1}	0.78

9-11	Equivalent Circuit	Fitted frequency range (Hz)	χ^2
T=190 K	$(R_1Q_1)(R_2Q_2)Q_3$	$0.46 – 2.79 \times 10^6$	1.75×10^{-3}
	Circuit Element	Value	Error %
	R_1	6.09×10^4	6.84
	Q_1	1.64×10^{-10}	19.48
	n_1	8.58×10^{-1}	1.74
	R_2	4.69×10^4	13.44
	Q_2	4.05×10^{-8}	63.23
	n_2	6.88×10^{-1}	12.91
	Q_3	3.30×10^{-6}	4.67
	n_3	6.44×10^{-1}	4.11

9-12	Equivalent Circuit	Fitted frequency range (Hz)	χ^2
T=190 K	$(R_1Q_1)(R_2Q_2)Q_3$	$0.055 – 5.18 \times 10^6$	2.46×10^{-3}
	Circuit Element	Value	Error %
	R_1	6.07×10^5	17.63
	Q_1	1.00×10^{-10}	23.61
	n_1	9.54×10^{-1}	2.79
	R_2	1.36×10^7	2.55
	Q_2	2.70×10^{-10}	12.26
	n_2	8.85×10^{-1}	2.21
	Q_3	1.78×10^{-7}	6.24
	n_3	6.63×10^{-1}	5.94

10-11	Equivalent Circuit	Fitted frequency range (Hz)	χ^2
T=190 K	$(R_1Q_1)(R_2Q_2)$	$0.093 – 7.00 \times 10^6$	9.13×10^{-3}
	Circuit Element	Value	Error %
	R_1	5.66×10^6	16.34
	Q_1	1.64×10^{-11}	35.90
	n_1	1.00	3.61
	R_2	2.05×10^8	2.77
	Q_2	1.11×10^{-10}	7.94
	n_2	8.64×10^{-1}	1.66

10-12	Equivalent Circuit	Fitted frequency range (Hz)	χ^2
T=190 K	$(R_1Q_1)(R_2Q_2)$	$7.99 – 2.28 \times 10^4$	1.63×10^{-4}
	Circuit Element	Value	Error %
	R_1	2.85×10^6	11.55
	Q_1	4.17×10^{-11}	14.28
	n_1	9.86×10^{-1}	2.15
	R_2	1.68×10^7	2.53
	Q_2	2.36×10^{-10}	5.29
	n_2	8.39×10^{-1}	1.58

11-12	Equivalent Circuit	Fitted frequency range (Hz)	χ^2
T=190 K	$(R_1Q_1)Q_2$	$0.019 – 2.69 \times 10^6$	7.57×10^{-4}
	Circuit Element	Value	Error %
	R_1	6.81×10^5	0.50
	Q_1	9.95×10^{-11}	3.88
	n_1	8.81×10^{-1}	0.31
	Q_2	3.42×10^{-6}	1.81
	n_2	8.88×10^{-1}	0.96

9-10	Equivalent Circuit	Fitted frequency range (Hz)	χ^2
T=300 K	$R_0(R_1Q_1)\ Q_2$	$0.86 – 1.12x10^5$	$5.47x10^{-5}$
	Circuit Element	Value	Error %
	R_0	$1.38x10^1$	0.23
	R_1	3.75	38.11
	Q_1	$1.92x10^{-4}$	65.09
	n_1	1.00	8.93
	Q_2	$1.84x10^{-5}$	0.49
	n_2	$8.95x10^{-1}$	0.15

9-11	Equivalent Circuit	Fitted frequency range (Hz)	χ^2
T=300 K	$R_0(R_1Q_1)(R_2Q_2)Q_3$	$0.1 – 3.28x10^5$	$2.33x10^{-4}$
	Circuit Element	Value	Error %
	R_0	3.61	1.59
	R_1	8.66	50.08
	Q_1	$1.44x10^{-4}$	42.98
	n_1	$6.98x10^{-1}$	10.19
	R_2	$5.51x10^1$	33.50
	Q_2	$1.08x10^{-3}$	41.31
	n_2	$5.84x10^{-1}$	17.23
	Q_3	$2.30x10^{-4}$	0.55
	n_3	$7.92x10^{-1}$	0.59

9-12	Equivalent Circuit	Fitted frequency range (Hz)	χ^2
T=300 K	$R_0(R_1Q_1)Q_2$	$1.50 – 3.45x10^8$	$2.79x10^{-5}$
	Circuit Element	Value	Error %
	R_0	$6.15x10^1$	0.45
	R_1	$4.58x10^2$	2.20
	Q_1	$1.02x10^{-5}$	3.94
	n_1	$6.19x10^{-1}$	0.60
	Q_2	$2.66x10^{-6}$	0.39
	n_2	$7.92x10^{-1}$	0.12

10-11	Equivalent Circuit	Fitted frequency range (Hz)	χ^2
T=300 K	R_1Q_1	$0.18 – 1.12x10^5$	$7.46x10^{-4}$
	Circuit Element	Value	Error %
	R_1	$1.30x10^1$	0.79
	Q_1	$1.27x10^{-5}$	0.90
	n_1	$9.15x10^{-1}$	0.17

10-12	Equivalent Circuit	Fitted frequency range (Hz)	χ^2
T=300 K	$R_0(R_1Q_1)(R_2Q_2)Q_3$	$0.33 – 5.49x10^5$	$1.34x10^{-4}$
	Circuit Element	Value	Error %
	R_0	$3.65x10^1$	0.51
	R_1	$5.03x10^2$	30.20
	Q_1	$1.47x10^{-6}$	9.37
	n_1	$8.69x10^{-1}$	3.43
	R_2	$1.10x10^3$	21.09
	Q_2	$5.52x10^{-6}$	23.94
	n_2	$8.40x10^{-1}$	9.49
	Q_3	$3.97x10^{-6}$	0.65
	n_3	$8.84x10^{-1}$	0.33

11-12	Equivalent Circuit	Fitted frequency range (Hz)	χ^2
T=300 K	$R_0(R_1Q_1)Q_2$	$1.2 – 2.84x10^4$	$1.69x10^{-4}$
	Circuit Element	Value	Error %
	R_0	$1.34x10^1$	0.59
	R_1	$4.27x10^1$	25.42
	Q_1	$3.36x10^{-5}$	32.07
	n_1	1.00	5.43
	Q_2	$1.05x10^{-5}$	0.99
	n_2	$8.64x10^{-1}$	0.35

Table S3 Fitted equivalent circuits for the spectra showed in Figure S12 and S13. Q and *n* represent the modulus and the exponent of the constant phase element.

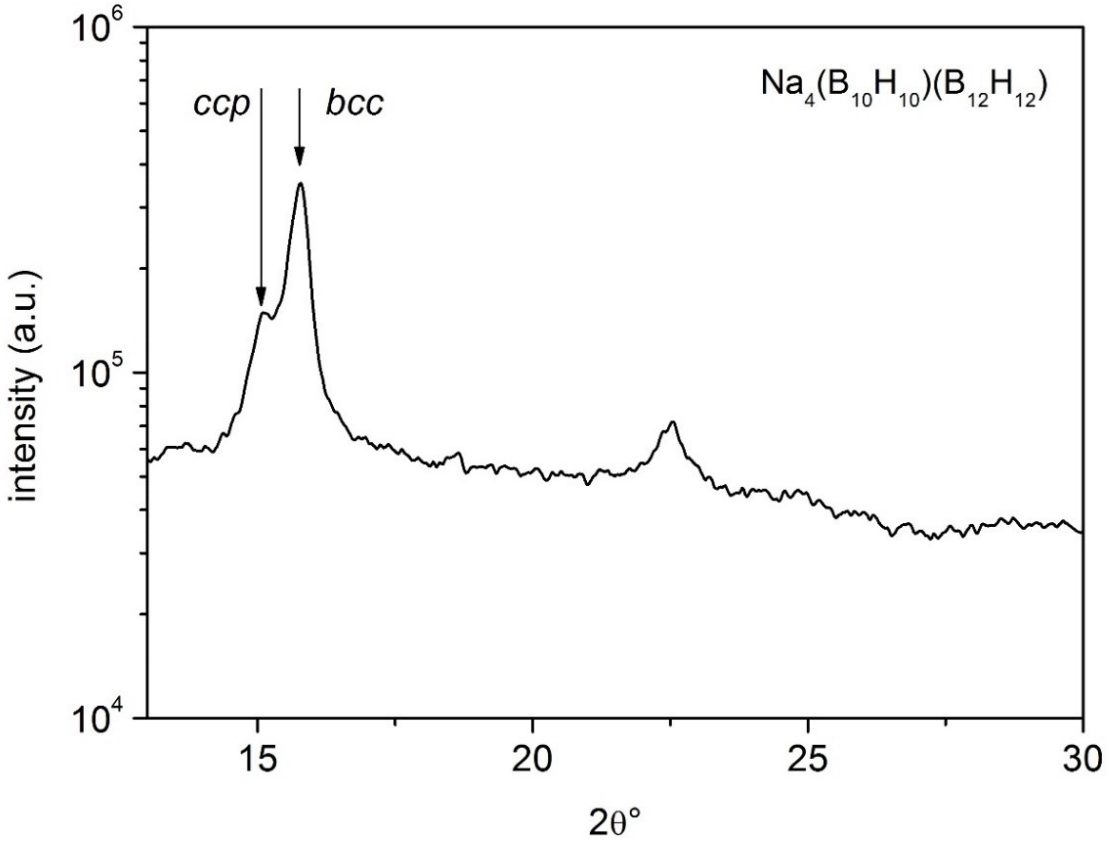

Figure S14 XRD profile of $Na_4(B_{10}H_{10})(B_{12}H_{12})$ measured with laboratory diffractometer. Data were collected at T=298 K, $\lambda = Cu_{K\alpha 1}$, both (111) and (110) peaks of *ccp* and *bcc* phases are clearly present at about 16° of 2θ.

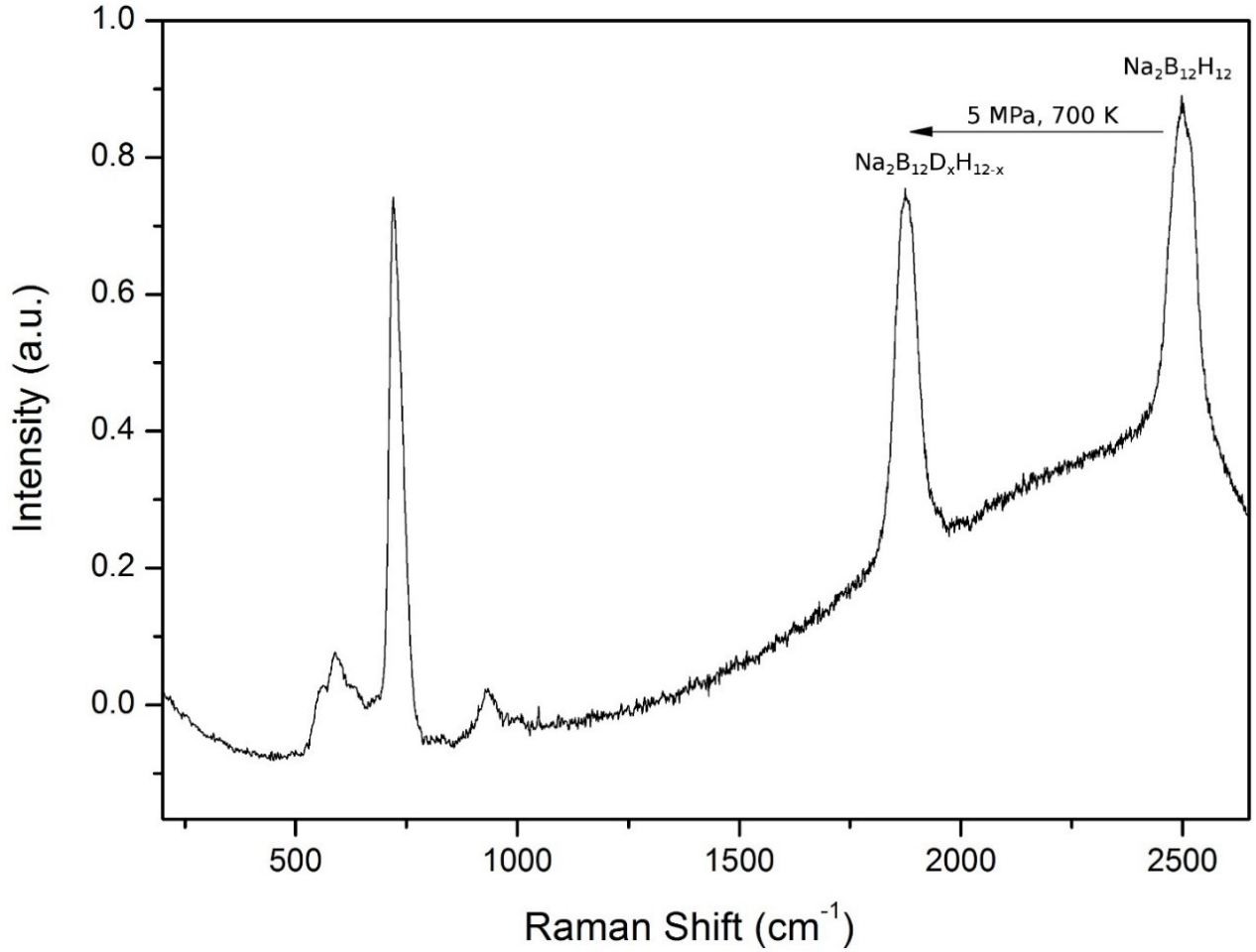

Figure S15 Raman spectra collected at *rt* for the sample $Na_2B_{12}H_{12-x}D_x$. The band centred at 716 cm^{-1} represents the B-H bending mode, while those at higher wavenumbers the B-D and B-H stretching mode (1880 and 2500 cm^{-1} respectively).
The result of isotopic exchange of $Na_2B_{12}H_{12}$ obtained by Raman spectroscopy is shown in Figure S15. The substitution lead to a shift of the band centred at 2500 cm^{-1} to 1880 cm^{-1}, corresponding to the frequency change of the B-H stretching mode due to the H-D replacement,[2,3] while the band around 716 cm^{-1}, related to the bending mode, results unchanged.

Supplemental References

[1] Y. Sadikin, P. Schouwink, M. Brighi, Ł. Zbigniew, R. Cerny, *Inorg. Chem.* **2017**, *56*, 5006.

[2] M. Sharma, D. Sethio, V. D'Anna, J. C. Fallas, P. Schouwink, R. Černý, H. Hagemann, *J. Phys. Chem. C* **2015**, *119*, 29.

[3] D. Sethio, L. M. Lawson Daku, H. Hagemann, *Int. J. Hydrogen Energy* **2017**, *42*, 22496.